Global Assessment of Mesoscale Eddies with TOEddies: Comparison Between Multiple Datasets and Colocation with In Situ Measurements

Artemis Ioannou, Lionel Guez, Rémi Laxenaire, Sabrina Speich

remote sensing

MDPI

Article

Global Assessment of Mesoscale Eddies with TOEddies: Comparison Between Multiple Datasets and Colocation with In Situ Measurements

Artemis Ioannou [1,*], Lionel Guez [1], Rémi Laxenaire [1,2,3] and Sabrina Speich [1,4]

[1] École Normale Supérieure, Laboratoire de Météorologie Dynamique, LMD-IPSL, 24 rue Lhomond, 75005 Paris, France; guez@lmd.ipsl.fr (L.G.)
[2] Laboratoire de L'Atmosphere et des Cyclones (LACy), UMR 8105 CNRS, Universite de La Reunion, Meteo-France, 97744 Saint-Denis, France
[3] Center for Ocean-Atmospheric Prediction Studies, Florida State University, Tallahassee, FL 32310, USA
[4] École Normale Supérieure ENS-PSL, 24 rue Lhomond, 75005 Paris, France
* Correspondence: artemis.ioannou@lmd.ipsl.fr

Abstract: The present study introduces a comprehensive, open-access atlas of mesoscale eddies in the global ocean, as identified and tracked by the TOEddies algorithm implemented on a global scale. Unlike existing atlases, TOEddies detects eddies directly from absolute dynamic topography (ADT) without spatial filtering, preserving the natural spatial variability and enabling precise, high-resolution tracking of eddy dynamics. This dataset provides daily information on eddy characteristics, such as size, intensity, and polarity, over a 30-year period (1993–2023), capturing complex eddy interactions, including splitting and merging events that often produce networks of interconnected eddies. This unique approach challenges the traditional single-trajectory perspective, offering a nuanced view of eddy life cycles as dynamically linked trajectories. In addition to traditional metrics, TOEddies identifies both the eddy core (characterized by maximum azimuthal velocity) and the outer boundary, offering a detailed representation of eddy structure and enabling precise comparisons with in situ data. To demonstrate its value, we present a statistical overview of eddy characteristics and spatial distributions, including generation, disappearance, and merging/splitting events, alongside a comparative analysis with existing global eddy datasets. Among the multi-year observations, TOEddies captures coherent, long-lived eddies with lifetimes exceeding 1.5 years, while highlighting significant differences in the dynamic properties and spatial patterns across datasets. Furthermore, this study integrates TOEddies with 23 years of colocalized Argo profile data (2000–2023), allowing for a novel examination of eddy-induced subsurface variability and the role of mesoscale eddies in the transport of global ocean heat and biogeochemical properties. This atlas aims to be a valuable resource for the oceanographic community, providing an open dataset that can support diverse applications in ocean dynamics, climate research, and marine resource management.

Keywords: mesoscale eddies; remote sensing; satellite altimetry; eddy tracking methods; subsurface oceanic signal; eddy–eddy interactions; merging–splitting events; coherent eddies; eddy networks

Citation: Ioannou, A.; Guez, L.; Laxenaire, R.; Speich, S. Global Assessment of Mesoscale Eddies with TOEddies: Comparison Between Multiple Datasets and Colocation with In Situ Measurements. *Remote Sens.* **2024**, *16*, 4336. https://doi.org/10.3390/rs16224336

Academic Editor: Angelo Perilli and Mariona Claret

Received: 4 October 2024
Revised: 5 November 2024
Accepted: 11 November 2024
Published: 20 November 2024

1. Introduction

Mesoscale eddies are fundamental to the transport and distribution of oceanic properties, significantly influencing global water mass movement, energy, heat, salt and biogeochemical fluxes across large horizontal and vertical scales [1–8]. These dynamic structures, often retaining their coherence over extended periods, play a crucial role in mediating exchanges between the surface and subsurface ocean [9–11]. As they propagate through the ocean, mesoscale eddies act as reservoirs, trapping water masses and preserving their internal characteristics, contributing to complex exchanges that influence biological productivity and ocean–atmosphere interactions [12–16].

The global monitoring of mesoscale eddy dynamics, however, remains constrained by the limitations of satellite-based altimetric coverage. While multi-mission altimeters provide essential data for tracking sea surface height (SSH), these measurements capture the mesoscale only indirectly, leaving gaps in higher-resolution observations and introducing mapping uncertainties due to sparse temporal sampling. Gridded SSH fields are reconstructed through spatiotemporal interpolation over intervals typically lasting several days [17], which restricts the fidelity of smaller-scale features and rapidly evolving dynamics [18]. Despite these limitations, satellite altimetry—particularly absolute dynamic topography (ADT) and sea level anomaly (SLA) data—continues to be the primary method for detecting and analyzing mesoscale eddies, given its resilience to cloud cover and nearly continuous oceanic coverage [19–21]. Integrating altimetric data with in situ observations from oceanographic campaigns has also been shown to enhance mesoscale eddy detection and provide more detailed insights into their dynamics and vertical structures [22–24].

Historically, SLA maps have served as the basis for numerous global eddy studies, offering comprehensive insights into eddy statistics and variability Chelton et al. [10,25]. However, approaches to eddy detection vary significantly, ranging from physical and geometric methods to hybrid techniques that apply spatial filtering to isolate mesoscale signals [10,26–34]. Recent algorithms have introduced methods to track complex eddy behaviors, such as merging and splitting events, which reveal interconnected networks of eddy pathways rather than isolated trajectories [4,30,35,36]. Nonetheless, only a handful of atlases offer publicly accessible, global-scale, long-term datasets for mesoscale eddy monitoring, and few consider eddy interactions like merging or splitting on a global scale [4,36]. Such information is critical for accurately capturing eddy lifetimes, transport properties, and spatial distributions, which are necessary for a deeper understanding of their impacts on ocean circulation and water mass exchanges.

In this study, we present the enhanced, global version of the TOEddies atlas—a mesoscale eddy detection and tracking dataset [37] designed to overcome some limitations of existing global atlases. TOEddies distinguishes itself in four fundamental ways: (1) it operates directly on ADT fields without spatial filtering, allowing it to detect mesoscale eddies influenced by both barotropic and baroclinic dynamics; (2) it captures the complex behavior of eddy networks by tracking splitting and merging events, thus offering a more intricate perspective on eddy pathways beyond linear trajectories; (3) it differentiates the outermost eddy boundary from the core, defined by the maximum azimuthal velocity, facilitating a more detailed examination of eddy structure; and (4) it integrates Argo float measurements to assess the vertical structure and thermohaline properties within eddies, introducing novel possibilities for characterizing eddy internal variability across the global ocean. While numerous regional and global studies have previously colocalized satellite-derived eddy features with Argo profiles or ship-based hydrography, no existing atlas has systematically incorporated this feature. This integration of satellite and in situ data provides a unique resource for exploring interactions between surface and subsurface oceanic processes.

Following a presentation of the TOEddies dataset, we conduct a comparative analysis with three widely used global eddy atlases [34,38,39], evaluating key mesoscale characteristics such as eddy spatial distributions, size, intensity, and pathways. Additionally, we analyze the differences in eddy lifetimes and propagation characteristics observed across datasets and explore the implications of these differences for oceanographic research.

The structure of this paper is as follows: Section 2 presents the TOEddies algorithm and details the data sources used in this study. Section 3.1 examines the statistical properties and spatial distributions of mesoscale eddies across the global ocean as detected by the various atlases. In Section 3.2, we compare the primary eddy pathways and assess the evolution of long-lived eddies. Section 3.3 introduces the new eddy-network framework offered by TOEddies, highlighting merging and splitting events and presenting specific eddy examples captured in conjunction with Argo observations. Lastly, we summarize our findings and discuss the significance of these results in Section 4.

2. Materials and Methods

This study evaluates four global mesoscale eddy atlases to examine the global structure and dynamics of mesoscale eddies. At the core of our analysis is the TOEddies Atlas, initially developed for the South Atlantic [4,5,40] and now expanded to cover the global ocean [37]. TOEddies has undergone extensive validation and has been employed in over 20 peer-reviewed studies, highlighting its robustness and practical utility for eddy characterization [7,15,22–24,41–49]. It has also been used in several large-scale scientific missions, including EUREC4A-OA and the Tara Mission, further demonstrating its relevance within the oceanographic community [24,48,50,51]. In addition to TOEddies, we examine the latest version of the Mesoscale Eddy Trajectory Atlas META (version 3.2), as described in [34] and available from AVISO+ with support from CNES (http://www.aviso.altimetry.fr/, 10.24400/527896/a01-2022.005, accessed on 5 November 2024). This version of META spans 29 years (from January 1993 to February 2022) and applies daily eddy detection based on absolute dynamic topography (ADT) fields (Table 1). To broaden our comparative analysis, we also include eddy detection and tracking outputs from Tian et al. [38] (http://coadc.ouc.edu.cn/tfl/, accessed on 5 November 2024), which are based on the AVISO all-satellite dataset of sea level anomaly (SLA) for the period 1993–2016, hereafter referred to as TIAN. Finally, we incorporate the recent GOMEAD dataset [39], which provides eddy detection and tracking using SLA fields, covering the period from January 1993 to December 2019.

Table 1. Overview of eddy detection datasets.

Dataset	SSH (All-Sat)	Threshold	Period
TOEddies	ADT	0.1 cm	Janurary 1993–May 2023
META3.2	ADT	0.4 cm	Janurary 1993–September 2022
TIAN	SLA	0.25 cm	Janurary 1993–December 2016
GOMEAD	SLA	-	Janurary 1993–December 2019

2.1. Eddy Atlases and Sea Surface Height Data

All atlases utilized in this study are derived from daily, multi-satellite sea surface height fields produced by Copernicus Marine Service (https://marine.copernicus.eu/fr, 10.48670/moi-00148, accessed on 5 November 2024). This specific multi-satellite product integrates data from up to eight satellites at a given time and is projected onto a Cartesian grid with a resolution of $\frac{1}{4}^{\circ}$ covering the global ocean. Each dataset evaluates mesoscale eddies using either absolute dynamic topography (ADT) or sea level anomaly (SLA) (Table 1), derived from gridded maps generated within a time-delay framework. ADT is the preferred measure in TOEddies and META3.2 as it avoids misinterpretations of the mean dynamic topography (MDT) and large meanders as eddies [4,34]. In contrast, SLA is often filtered to remove large-scale features and is commonly applied in TIAN and GOMEAD.

Unlike most datasets that apply filtering, TOEddies uses the full unfiltered ADT fields, preserving all observed altimetric signals and thus ensuring a broader capture of mesoscale and submesoscale dynamics. For this reason, TOEddies is particularly adept at identifying both barotropic and baroclinic components of the eddy fields.

2.2. Eddy-Amplitude Thresholds and Core Structure Definition

Each Atlas employs different physical and geometric criteria to detect and track eddies. As a result, we have identified a number of key differences between the datasets. For a comprehensive understanding of the TOEddies detection and tracking method, please refer to Appendix A.1.

Eddies are identified as maximum or minimum points in the sea surface height (SSH) fields. Cyclonic eddies correspond to local minima of SSH, while anticyclonic eddies correspond to local maxima. Each dataset utilizes a unique threshold for eddy amplitude, commonly known as the persistence parameter [4], influencing both the number of detected

eddies and their derived properties. The TOEddies method uses a low threshold of 1 mm, which was empirically validated through comparisons with independent surface drifter datasets [52]. In the META3.2 and TIAN datasets, the eddy amplitude criterion is set to 0.4 cm and 0.25 cm, respectively (see Table 1).

Typically, the eddy detection process begins with the identification of maxima and minima across the field, which is then followed by the application of the specified amplitude thresholds. In a different approach, TOEddies incorporates the persistence parameter directly into the detection process. This integrated approach is topologically distinct and has been shown to enhance eddy detection, functioning as a low-pass filter [4]. The latter has been validated against a totally independent dataset of upper-ocean eddies identified by surface drifters and provided by Lumpkin [52]. For each local extreme, TOEddies identifies the outermost and maximum-speed contour of ADT that satisfy the specified constraints detailed in Appendix A.1.

An alternative approach is employed by the GOMEAD atlas, which utilizes a vector geometry-based algorithm for the detection of eddies. This methodology identifies eddy centers as local minima of the surface geostrophic velocity magnitude derived from the SLA, and delineates eddy boundaries through the utilization of isolines of the geostrophic stream function.

2.3. Eddy Tracking Approaches

To monitor eddies over time, both META3.2 and TOEddies employ an overlapping criterion between successive time steps, as previously introduced in Pegliasco et al. [53]. This criterion guarantees that a defined area of the eddy remains consistent between consecutive time steps. This approach allows us to identify distinct segments of eddies, rather than isolated occurrences, which is essential for reconstructing eddy trajectories. In TOEddies, a graph method has been implemented to identify eddy segments and build eddy trajectories, enabling the detection of merging and splitting events. This is achieved by integrating a cost function that assigns weights to the graph of segments, taking into account three key similarity parameters: the distance between eddies, their Rossby numbers, and their speed radius. Please refer to Appendix A.2 for further details regarding the TOEddies tracking methodology. Please note that META3.2 does not include the identification of merging and splitting events.

In contrast, the TIAN dataset links trajectories over time by identifying each eddy at the current time step and searching for an eddy in the subsequent time step within a fixed area of radius 0.5°. In the event that an eddy remains unassociated in the subsequent step, a synthetic or "fake" eddy with similar attributes to the last observed eddy is created. The synthetic eddy is then introduced into the fields and propagated in the same direction. This technique, originally proposed by Faghmous et al. [27], helps to prevent the premature termination of tracks or large jumps between eddy positions. The maximum number of steps that fake eddies are permitted in TIAN is set at five days, while their propagation distances cannot exceed 1.75 times the distance over which a long baroclinic Rossby wave can propagate in a week. In the event that multiple eddies fall into the same area, a cost function is employed that considers four similarity parameters: distance between eddies, amplitudes, area, and EKE. META3.2 and TOEddies also prevent the disappearance of eddies by extending this search to four (META3.2) or six (TOEddies) time steps if no eddy has been found before. Lastly, GOMEAD implements a similar fixed search area approach to track eddies over time. If multiple eddies of the same type are detected within the search area, the eddy track is updated by selecting the center point that is closest to the eddy.

2.4. Eddy-Network and Interaction Mapping

The TOEddies atlas uniquely reconstructs networks of eddy interactions. This network-based approach not only captures traditional eddy trajectories but also records merging and splitting events, offering insights into connectivity and cross-basin transport. The capability of TOEddies to detect eddy merging and splitting events enables the reconstruc-

tion of eddy networks linked to specific eddy origins. This methodology, introduced in Laxenaire et al. [4,5,40], allows for continuous monitoring of eddy evolution, capturing interactions that occur throughout an eddy's lifetime. The TOEddies network tracks interactions between oceanic eddies by detecting merging and splitting events, assigning an "order" to each trajectory (see Figure 1 in Laxenaire et al. [40]). A reference eddy trajectory, originating from a specific region, is assigned an order of zero, while eddies that merge with or split from this reference are assigned orders based on the number of interactions separating them from the original trajectory. This network-based approach provides a novel way to trace eddy origins, pathways and cross-basin connectivity [4,7,24]. By accounting for multiple merging or splitting events, the TOEddies network provides a more detailed and dynamic reconstruction of eddy movements compared to conventional methods, which consider eddies as isolated structures.

2.5. Integration with Argo Data

To capture the vertical structure of eddies, TOEddies [37] is integrated with Argo float profiles from 2000 to 2023, totaling nearly 3 million profiles (2,786,034) from over 17,000 floats (17,733), 10% of which (2336) are biogeochemical (BGC-Argo). The Argo profiles are separated into two groups based on their detection within or outside of mesoscale eddy last contours at a specific location and date. The latter represent the adjacent environment and are used to construct climatological profiles of temperature (T), salinity (S), and density (σ) in the given area. TOEddies colocalization provides a "no-eddy" climatology consisting of all profiles located outside of eddies within a $\leq 1^\circ$ radius and during a period of up to 30 days from the given date (regardless of the year) over the 23 years. This provides a comprehensive environmental baseline for comparison.

3. Results

3.1. Statistical Description of Mesoscale Eddies

Figure 1 presents a global characterization of mesoscale eddy activity. The figure shows the detection from each atlas accumulated on a $1^\circ \times 1^\circ$ gridded map, with areas of eddy generation and disappearance clearly delineated. The latter were identified as the initial and final detection points of each eddy trajectory that was monitored for a minimum of 4 weeks. The highest concentrations of eddy activity are defined by a high density of eddy generations and disappearances, with a total exceeding $N > 30$ eddies per degree square. It is notable that, in all datasets, areas where eddies frequently generate are also areas where eddies disappear from the altimetry maps. It is evident that the eastern boundary areas, including the major eastern upwelling boundary systems in the Canary and Benguela in the South Atlantic, as well as the western boundary near the confluence zone between the Malvinas and South Brazil currents, exhibit a higher number of eddy generations. Please refer to Figure S1 of the Supplementary Material for a visual representation of the higher number of eddy disappearances in the western boundary systems.

Figure 2 shows frequency maps of eddy–eddy interactions (merging and splitting events) identified by TOEddies. It is important to note that the spatial distribution of merging and splitting events, as identified by TOEddies, also occurs in similar locations. This reinforces the necessity of considering eddy–eddy interactions for comprehensive understanding of the detected eddies' dynamic evolution. Over the course of the observation period, approximately 3% of the detected eddies were found to be involved in merging and splitting events, with 52% of these classified as cyclonic eddies.

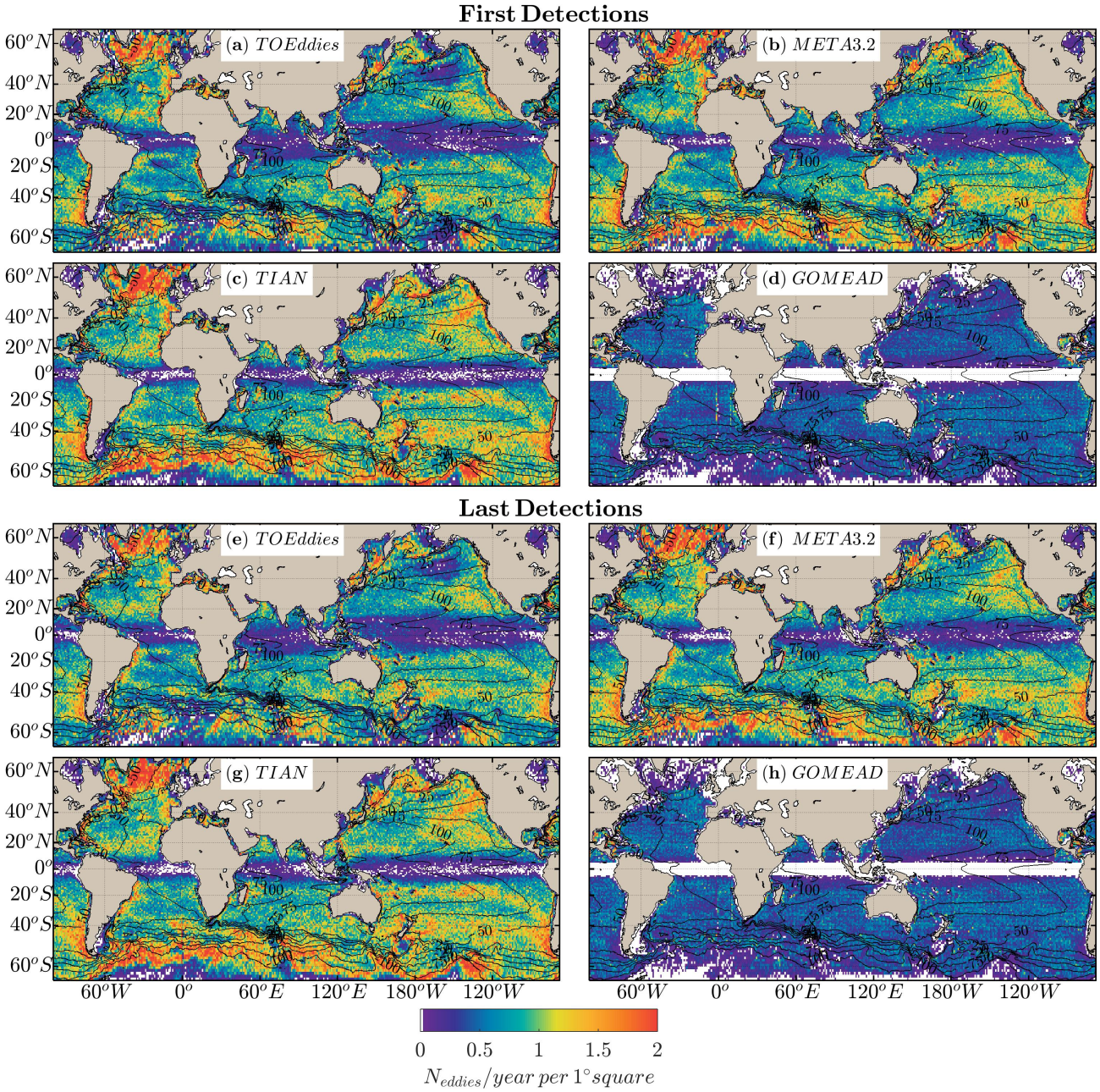

Figure 1. Frequency maps of first (**a**–**d**) and last (**e**–**h**) detection points of mesoscale eddies per year derived from TOEddies, META3.2, TIAN, and GOMEAD datasets, respectively. The data are aggregated into $1^\circ \times 1^\circ$ bins and normalized by the number of observation years for each dataset. The mean dynamic topography (MDT; in cm) is shown by black contours.

From the numerous mesoscale eddies identified across the global datasets over the various years of observation, we have chosen to focus on individual detections that are part of main eddy trajectories with lifetimes of at least 16 weeks. The TOEddies dynamical dataset detects over 25 million (25,117,786) eddy occurrences (lasting a minimum of 16 weeks) organized in 119,994 eddy trajectories globally. In terms of the same subset of tracked mesoscale eddies, TOEddies outperforms META3.2 and TIAN in terms of the number of total trajectories, with an increase of almost 2% and 18% (117,035 and 98,375). In comparison with the other datasets, GOMEAD reports a lower number of detected eddies (17,822).

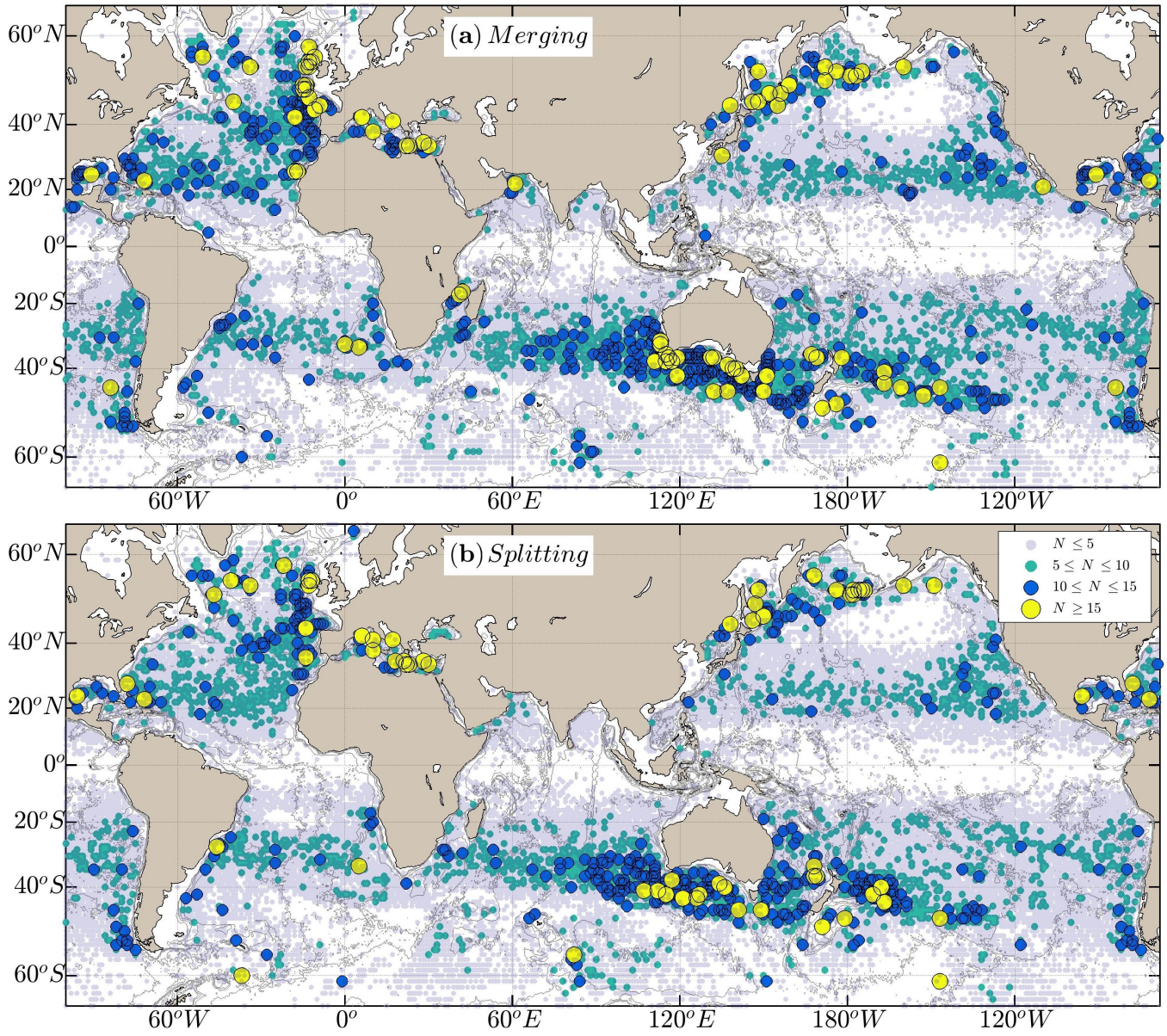

Figure 2. Scatter plot representing the distribution of eddy occurrences for (**a**) merging and (**b**) splitting events based on TOEddies atlas for eddies with lifetimes longer than 4 weeks in each $1° \times 1°$ region. Bathymetric contours at -500 m, -1000 m, -2000 m, and -4000 m are indicated by gray lines.

Figure 3 compares the horizontal eddy characteristics of each atlas. Histograms, of mesoscale eddy lifetimes, characteristic radii, and velocities are plotted separately for cyclonic and anticyclonic eddies. When longer lifetimes are considered (more than 26 weeks), the predominance of anticyclonic over cyclonic eddies becomes apparent, as noted in Chelton et al. [10]. Figure S3 of Supplementary Material illustrates this ratio, highlighting the significant differences in distribution between the two types of eddies.

In TOEddies and META3.2, the characteristic radii of anticyclonic eddies were estimated at $\langle R_{max} \rangle = 56.25\,(\pm 27.3)$ km and $\langle R_{max} \rangle = 62.08\,(\pm 27.8)$ km. These values of the equivalent average radii of the anticyclonic eddies in these atlases are 5% and 3% larger, respectively, in comparison to those of the cyclones. In the TIAN dataset, the anticyclonic eddy sizes are slightly larger, with an average radius of $\langle R_{max} \rangle = 68.86\,(\pm 27)$ km, while cyclones are 7% smaller in size. However, the relative size of the eddies in the TIAN

atlas remains larger than those identified in META3.2 and TOEddies. In general, the GOMEAD dataset identifies significantly larger structures (with an estimated average $\langle R_{max} \rangle = 109.5\,(\pm 45)$ km). We note that in this atlas, eddy radii smaller than ≤ 30 km are not included to avoid small-scale features that are not accurately captured by altimetry.

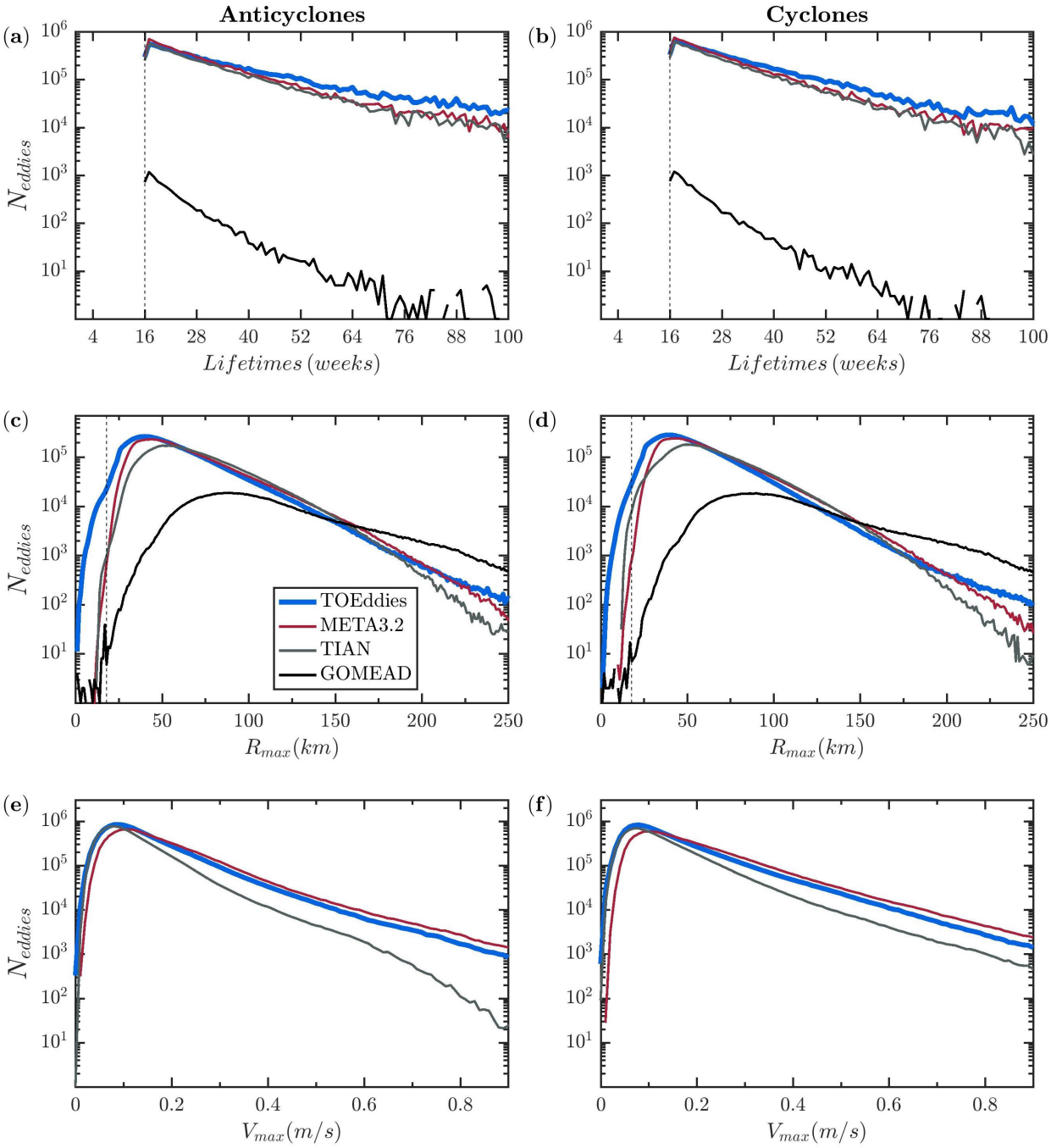

Figure 3. Histograms of eddy lifetimes (weeks) (**a**,**b**) and histograms of eddy characteristic radius R_{max} (km) (**c**,**d**) and velocity V_{max} (m/s) (**e**,**f**) of anticyclonic (first column) and cyclonic eddies (second column) for the TOEddies, META3.2, TIAN, and GOMEAD datasets. We consider only mesoscale eddies having lifetimes ≥ 16 weeks, as indicated by the dashed lines in panels (**a**–**d**), and characteristic radii larger than $R_{max} \geq 30$ km.

To identify areas where these differences are noticeable, in Figure 4 we present the geographical distribution of the radii of eddies. These maps were calculated by averaging

the R_{max} for each daily detected mesoscale eddy that falls within bins of 1° × 1°. For a suitable comparison, zonal averages of the eddy radius are also computed in Figure 4e. In terms of the spatial radius distribution, smaller eddies are detected near the poles and larger ones near the equator. This aligns with the first baroclinic Rossby radius, which varies with latitude [10,54]. However, the absolute values of the eddy radius vary considerably across the datasets. The mean zonal radii from the GOMEAD dataset are higher, estimated at approximately ~150 km in the equatorial bandwidth of 10°S to 10°N. In contrast, the TOEddies, META3.2, and TIAN datasets detect lower eddy radii of the order of 100–120 km. At latitudes lower than 40°S and higher than 40°N, the TIAN dataset identifies larger structures of approximately 60 km, while the TOEddies and META3.2 estimates indicate smaller structures (~40 km).

In terms of intensity, the mean characteristic velocities in the TOEddies dataset reaches almost $\langle V_{max} \rangle = 15\,(\pm 12)$ cm/s, while eddies in META3.2 and TIAN indicate slightly higher and lower velocities, $\langle V_{max} \rangle = 19\,(\pm 13)$ cm/s and $\langle V_{max} \rangle = 13\,(\pm 9)$ cm/s, respectively. It is worth noting that there are significant variations in the characteristics of the eddies, indicating that their sizes and intensities could differ significantly between observation periods. Furthermore, a comparison of all datasets reveals that cyclonic eddies display higher standard deviations in intensity than anticyclonic eddies.

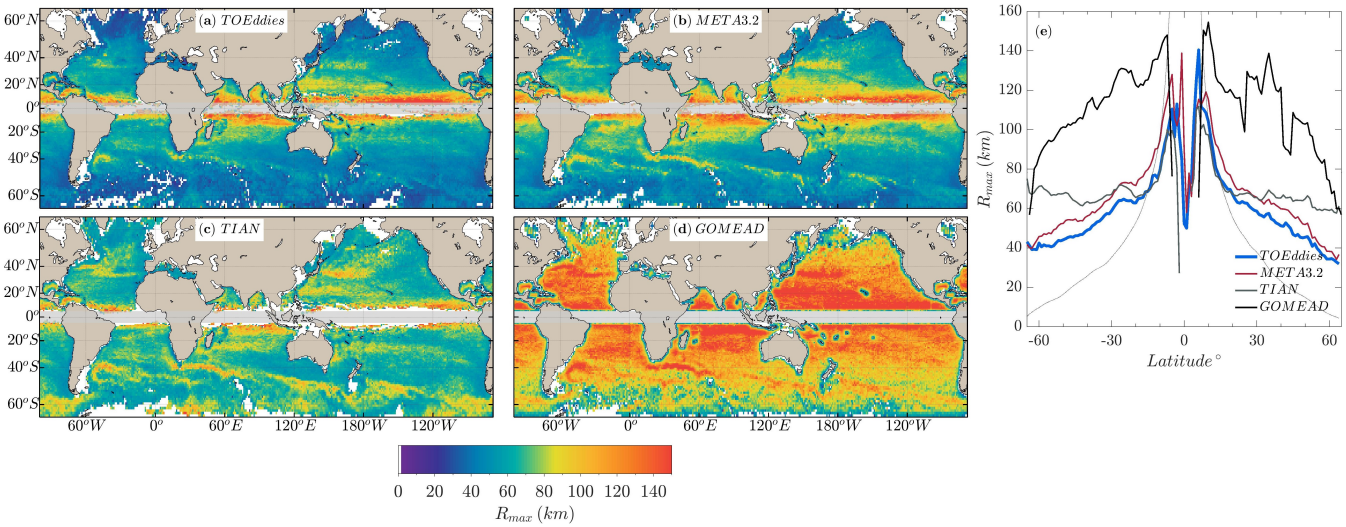

Figure 4. Maps of the speed-based radius scale R_{max} (km) for eddies with lifetimes ≥ 16 weeks for each 1° × 1° region from the (**a**) TOEddies, (**b**) META3.2, (**c**) TIAN, and (**d**) GOMEAD datasets. Zonal averages of the eddy characteristic radius are illustrated in panel (**e**). The dashed line indicates the estimated first baroclinic Rossby radius of deformation R_d (km) [10].

3.2. Characterization of Main Eddy Pathways

Figure 5 depicts eddy trajectories from the TOEddies atlas, based on their estimated lifetimes. The cyclonic and anticyclonic trajectories are presented separately, with blue and red colors, respectively. To facilitate a comparative analysis, we have selected similar thresholds as those chosen in Chelton et al. [10] for the eddy lifetimes. This results in lifetimes that exceed 52, 78, and 104 weeks, respectively. For instance, the selection of eddy trajectories that live longer than 78 weeks (more than 1.5 years) with the TOEddies dataset (Figure 5b) results in 2007 anticyclonic and 1339 cyclonic trajectories. In the North Atlantic, we find an equal eddy mixture of long-lived cyclones and anticyclones. However, in the Indian Ocean, we predominantly observe long-lived cyclones. These cyclones account for 40% of the total long-lived cyclones (for lifetimes ≥ 104 weeks) and are among the longest propagating eddies found in the TOEddies atlas.

Figure 6 shows the same selection of eddy trajectories (with lifetimes more than 78 weeks) with the META3.2, TIAN, and GOMEAD atlases. While both the META3.2 and TIAN atlases have a comparable number of persistent trajectories, their totals are 53%

and 41% lower, respectively, than that of TOEddies. For example, the META3.2 database includes 995 (773) anticyclonic (cyclonic) eddies with a lifetime exceeding 78 weeks, representing 56% (44%) of the total eddies. Similarly, the TIAN dataset contains 810 (564) anticyclonic (cyclonic) eddies, representing 59% (41%) of the total eddies. This discrepancy is primarily attributable to the lack of long-duration trajectories in the North and South Pacific. It is worth noting that the GOMEAD dataset identifies fewer trajectories than the other atlases. In fact, it contains 63 anticyclonic and 20 cyclonic eddies for this selection.

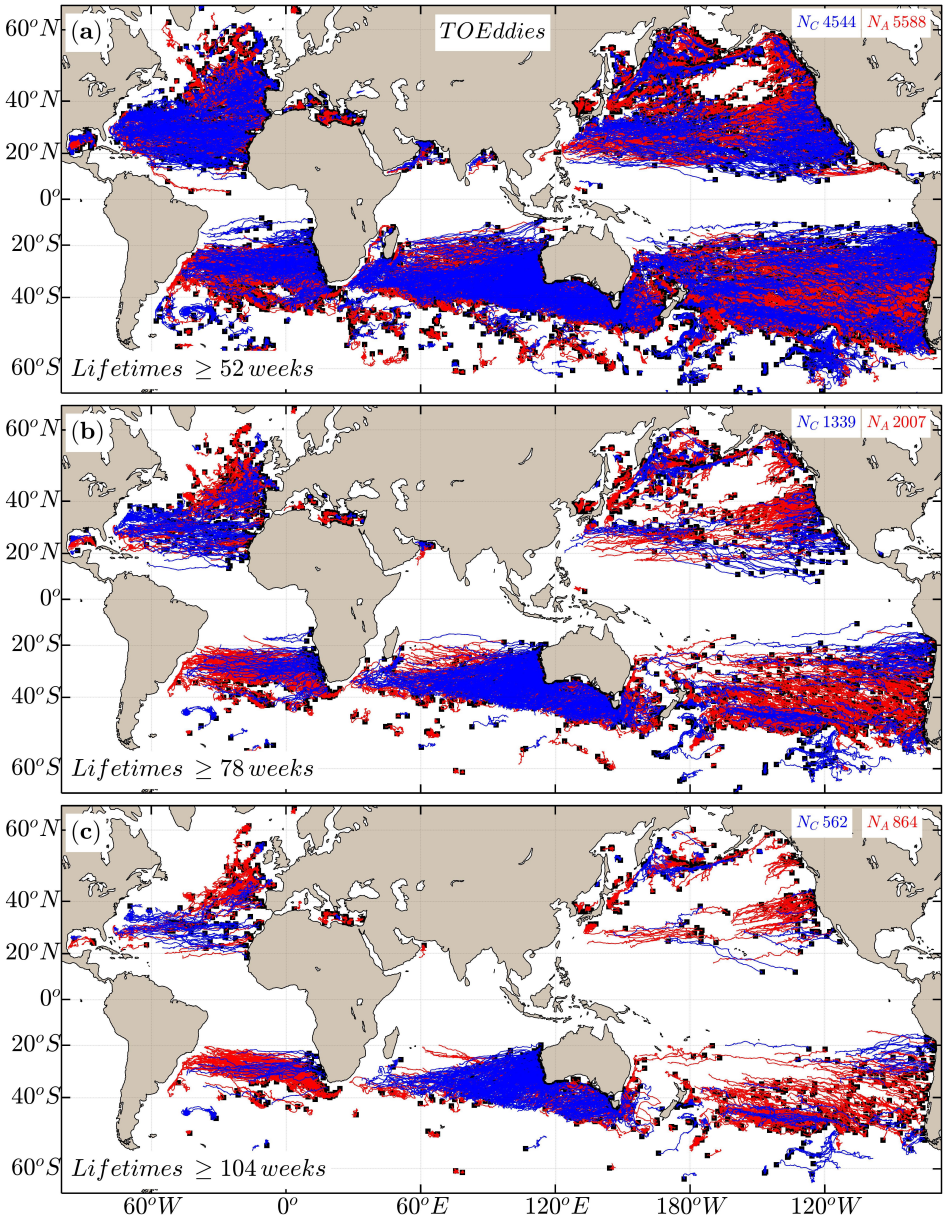

Figure 5. Cyclonic (blue) and anticyclonic (red) eddy trajectories as detected from the TOEddies algorithm having lifetimes of at least (**a**) ≥52 weeks, (**b**) ≥78 weeks, and (**c**) ≥104 weeks. The numbers of detected eddies are labeled at the top of each panel for each polarity.

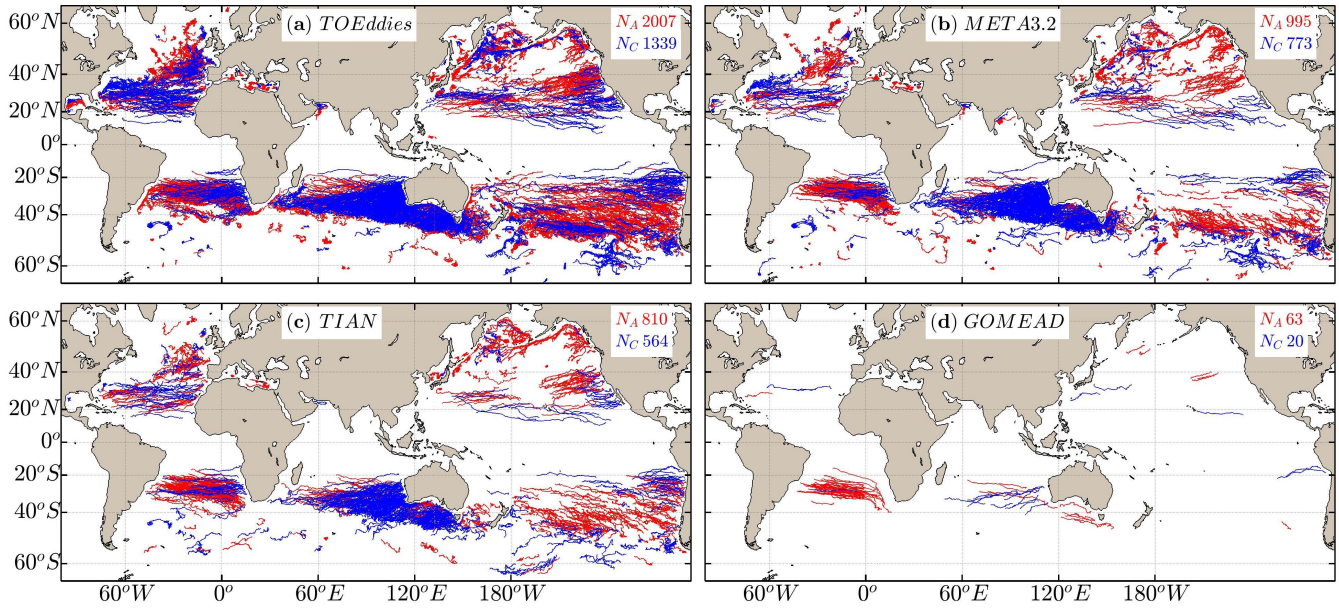

Figure 6. Trajectories of long-lived (≥78 weeks) cyclonic (blue) and anticyclonic (red) eddies from the (**a**) TOEddies, (**b**) META3.2, (**c**) TIAN, and (**d**) GOMEAD datasets. The numbers of eddies are labeled at the top of each panel for each polarity.

In alignment with Chelton et al. [10], all atlases indicate that the majority of long-lived oceanic eddies propagate in a westerly direction, influenced by the β-effect. Only a small fraction of eddies propagate eastward, particularly in regions dominated by strong currents, such as within the intense Antarctic Circumpolar Current (ACC) in the Southern Ocean. In regions where the background flow is weak, the differential Coriolis force leads anticyclonic eddies to drift equatorward and westward, while cyclonic eddies tend to drift poleward and westward [55,56]. This characteristic was consistently observed across all datasets, as shown in Figure S2 in the Supplementary Material. The proportion of eastward-propagating eddies is notably larger in the TIAN dataset. When lifetimes of less than 4 weeks are considered, the distribution of both westward and eastward eddies can reach as high as 50%, indicating an almost equal distribution. However, when eddies persist for at least 16 weeks, this ratio falls significantly to around 35%. TOEddies and META3.2 contain 20,061 and 30,440 eastward eddies, accounting for only 20% and 35% of the total eddies in the datasets.

It is also worth noting that there are differences in the behavior of long-distance propagating eddies between the eddy datasets. Figure 7 illustrates the trajectories of eddies from each dataset that were tracked for over 26 weeks and propagated over 1100 km. The distance was calculated for each eddy trajectory as the centroid distance between their initial and final positions, measured in kilometers. Long-lived, far-propagating eddies are of considerable interest to many studies due to their significant role in trapping and transporting water masses, along with heat, carbon, and oxygen. This process, in turn, influences global climate, marine connectivity, and ecosystem functioning [4,7,40,57]. The reliability of such estimates hinges on the precision with which mesoscale eddy temporal evolution and their en route interactions can be characterized. For example, the long-propagating Agulhas Rings leave a visible surface signature in the South Atlantic, which is reflected in all datasets. However, there are slight differences in the overview of the main eddy pathways depicted in each atlas, with some cases showing significant discrepancies. Such examples are visible mostly in the Pacific Ocean, where TOEddies detects more long-propagating eddies in the North Pacific, while only a portion of them is found in the TIAN dataset and META3.2 dataset (~11% and 46% fewer long-propagating trajectories, respectively). Large variations can also be observed in the South Pacific and North Atlantic.

To investigate in greater detail the consistency of long-lived eddies, we have focused our investigation on eddies with lifetimes of at least 26 weeks. We have then specifically targeted only those eddies that exhibited a consistent spatiotemporal evolution across all datasets. Given that the TOEddies dataset tracks a greater number of long-lived and long-propagating eddies, it was selected as the reference atlas. We then assessed the degree of similarity between the trajectories from the various datasets and the reference one. Eddies were classified as "similar" if, during the same temporal range, the average distance between their barycenters did not exceed a specified threshold, that we defined as $\geq 0.5°$. Our analysis revealed that the proportion of common eddy trajectories between TOEddies and the various datasets was approximately 72% for META3.2, 60% for TIAN, and only 25% for GOMEAD.

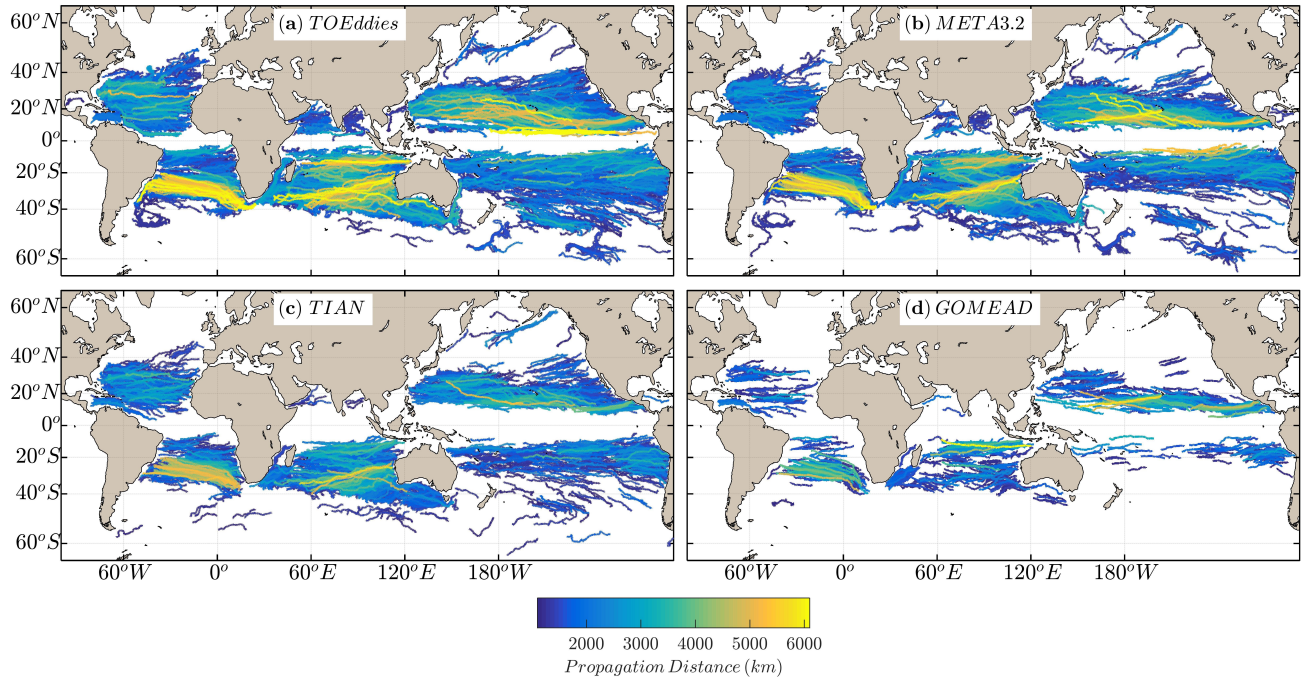

Figure 7. Trajectories of long-propagating (≥1100 km) eddies of both types from the (**a**) TOEddies, (**b**) META3.2, (**c**) TIAN, and (**d**) GOMEAD datasets tracked for ≥26 weeks.

3.3. Characterization of Main Eddy Interactions

It is crucial for any dataset aiming to represent mesoscale variability to have the capability to accurately track the temporal evolution of mesoscale eddies. It should be noted, however, that these large-scale mesoscale eddies are not isolated in the turbulent oceanic fields. Both anticyclonic and cyclonic eddies may undergo complex interactions along their dynamical evolution and can experience multiple merging or splitting events during their propagation. Such events modify the primary eddy pathways and are purported to be associated with substantial water transfers. It is, therefore, essential that merging and splitting events of both eddy types be identified so that the evolution of eddies can be understood.

The ability of TOEddies to determine the occurrence of eddy merging and splitting events enables the construction of unique eddy networks associated with specific eddy origins. In accordance with the methodology detailed in Laxenaire et al. [4,5,40], Figure 8 illustrates three eddy-network reconstructions as a case study. These are associated with the Agulhas Rings corridor, eddies originating from the North Pacific upwelling system, and eddies from the Australian western boundary. The trajectories in black, which originated from the area delineated by the dashed line, serve as the reference trajectories and are defined as order zero in the network (see Laxenaire et al. [4]). The order number is increased

with each additional interaction required to trace a reference trajectory in either direction. Consequently, these networks comprise all eddy trajectories that have encountered at least one merging or splitting event during their lifetime and, depending on their order, have connections to eddies of specific origins. The reconstruction of eddy networks indicates that long-lived and long-propagating eddies frequently interact with each other and have the potential to transport water from various regions of generation further away. To investigate the discrepancies among the different eddy atlases in tracking throughout the lifespan of eddies, an exhaustive analysis of two distinct long-lived eddies was conducted. The TOEddies algorithm incorporates the colocation of the eddies identified from the altimetry gridded field with available in situ measurements, thereby providing a valuable resource for in-depth studies of tracked eddies. To gain deeper insight into the vertical characteristics of these eddies and how they evolve over time, we identified individual eddy trajectories that were sufficiently sampled by Argo floats across the years of observation. In particular, we selected one anticyclonic eddy (A0) originating from the Agulhas leakage and one cyclonic eddy (C0) originating from the Australian western boundary, which were present in all datasets (Figure 9).

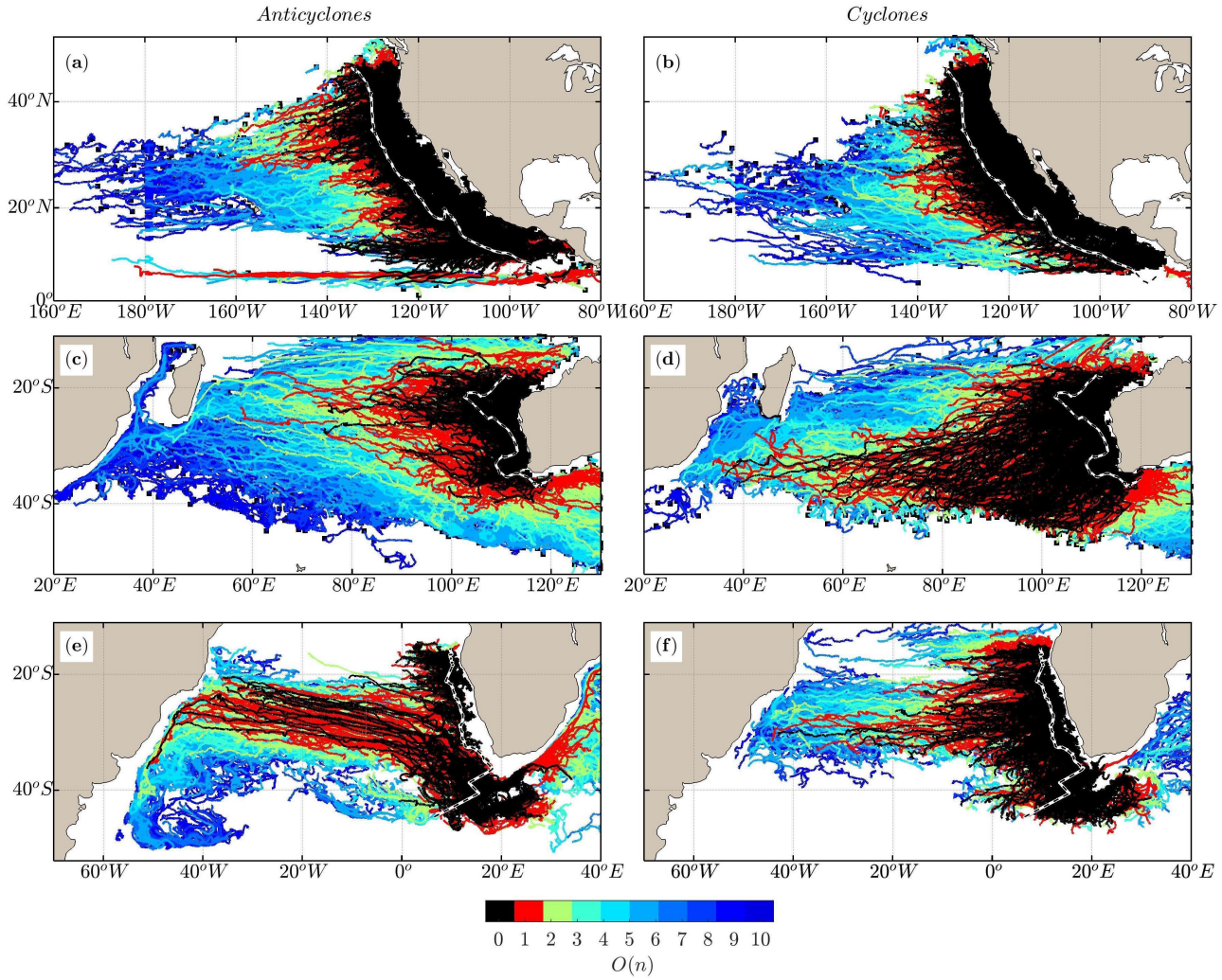

Figure 8. Eddy-network example of anticyclonic (first column) and cyclonic (second column) trajectories for the (**a**,**b**) California Upwelling System, (**c**,**d**) western Australian boundary, and (**e**,**f**) extended South Benguela System. Each eddy trajectory is colored according to its assigned order.

In Figure 9a,c, we present the specific trajectory network reconstruction of A0, which includes all eddies that have merged with and split from A0 during the three years of its

lifespan. Based on the TOEddies dataset, it can be concluded that A0 is the result of a splitting event that occurred in the Cape Basin on 11 September 2010 at (6.92°E, 32.88°S). Figure 10a shows that A0 originated from another anticyclone (A1) that was tracked back in the Agulhas retroflection as early as on 19 November 2009 (15.17°E, 37.40°S). During the period between October 2011 and January 2012, a number of complex interactions were observed in the Cape Basin, as illustrated in Figure 10b–d. After March 2011, A0 was observed crossing the Walvis Ridge and entering the South Atlantic, continuing westward at a consistent pace over 169 weeks (more than three years), up to 7 December 2013.

From October 2010 to September 2013, 20 Argo floats collected data from A0 at different radial distances from the core of the eddy. Figure 9a illustrates the temporal evolution of the A0 characteristic radii as computed by TOEddies applied to the ADT maps. In addition, the estimated distances of the Argo floats from the eddy core (magenta points, Figure 9a,b) are provided. The eddy defined by the R_{max} contour remains relatively constant, with a median value of 80 km and a standard deviation (STD), of 18.1 km. However, the outermost contour defining the eddy, R_{out}, shows important variations, ranging from 26 to 202 km and an STD of 34.3 km. Both META3.2 and TIAN identified the presence of eddy A0, as illustrated in Figure 9i. There is a noticeable overlap in the description of the main eddy pathway across all datasets. However, the TIAN algorithm identified a section of the eddy before its interaction with anticyclone A1, whereas the META3.2 dataset incorporated a portion of eddy A2 into the main trajectory.

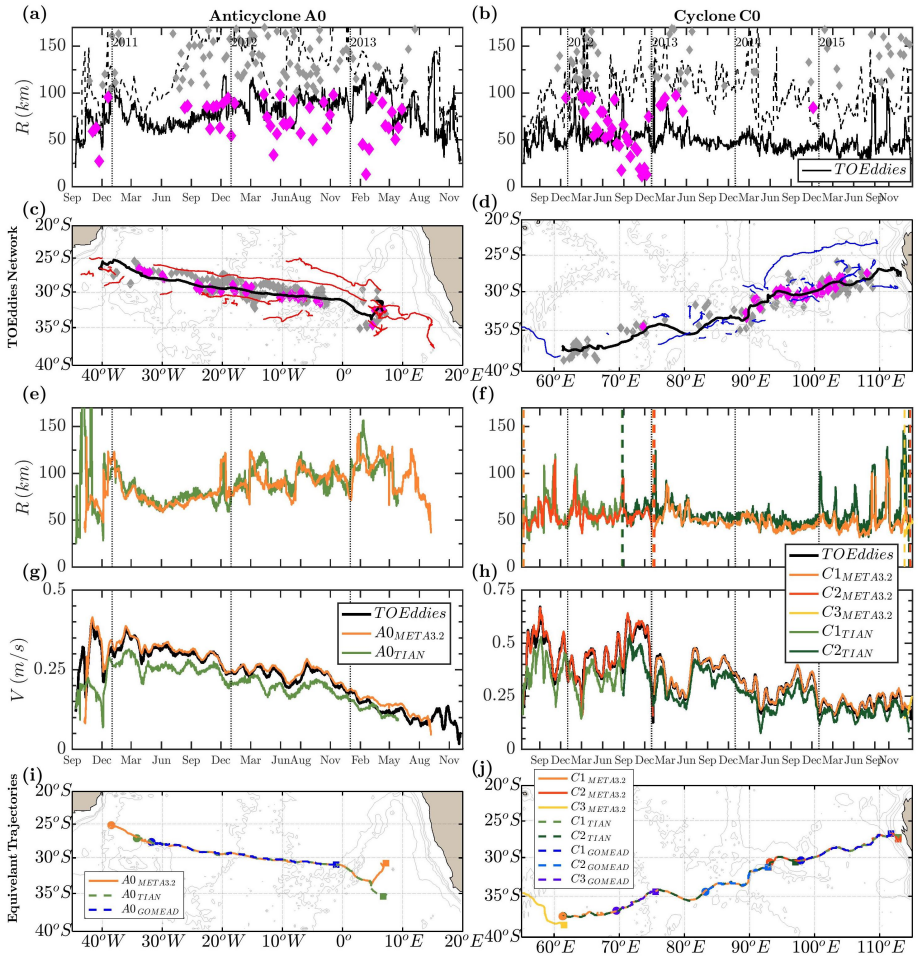

Figure 9. Temporal evolution of dynamical characteristics of anticyclone A0 and cyclone C0, as tracked by all considered datasets. The evolution of the eddy characteristic radius R_{max} (km) and outermost radius R_{out} (km) as tracked by TOEddies is shown in panel (**a**,**b**) for A0 and C0, respectively in black. The TOEddies network reconstruction composed of all detected trajectories,

The TOEddies network reconstruction composed of all detected trajectories, anticyclonic (red) and cyclonic (blue, that have merged and splitted with the main trajectories is shown in panels (**c**,**d**). The evolutions of the eddy radii and characteristic velocity V_{max} (m/s) from the different datasets are shown in panels (**e**–**h**). Panels (**i**,**j**) depict the equivalent A0 and C0 trajectories as tracked from the META3.2, TIAN, and GOMEAD datasets. Bathymetric contours at −500 m, −1000 m, −2000 m, and −4000 m are indicated by gray lines.

Figure 9e,g shows the temporal evolution of the anticyclone's characteristic radii and velocity across the various datasets. The temporal evolution of the eddy radius demonstrates a high level of similarity across the datasets, with mean differences with TOEddies of less than 6 km in META3.2 and 8 km in TIAN. Furthermore, the eddy V_{max} shows a consistent decline over time, a trend evident in all datasets. We observe a systematic decrease (in average 0.05 m/s), in the mean eddy intensity, as measured by TIAN, which is likely attributable to the use of SLA fields. However, while the decay of surface properties in the eddy indicates a distinct dissipation process, only the TOEddies atlas provides direct access to this information by integrating available hydrographic properties from Argo floats.

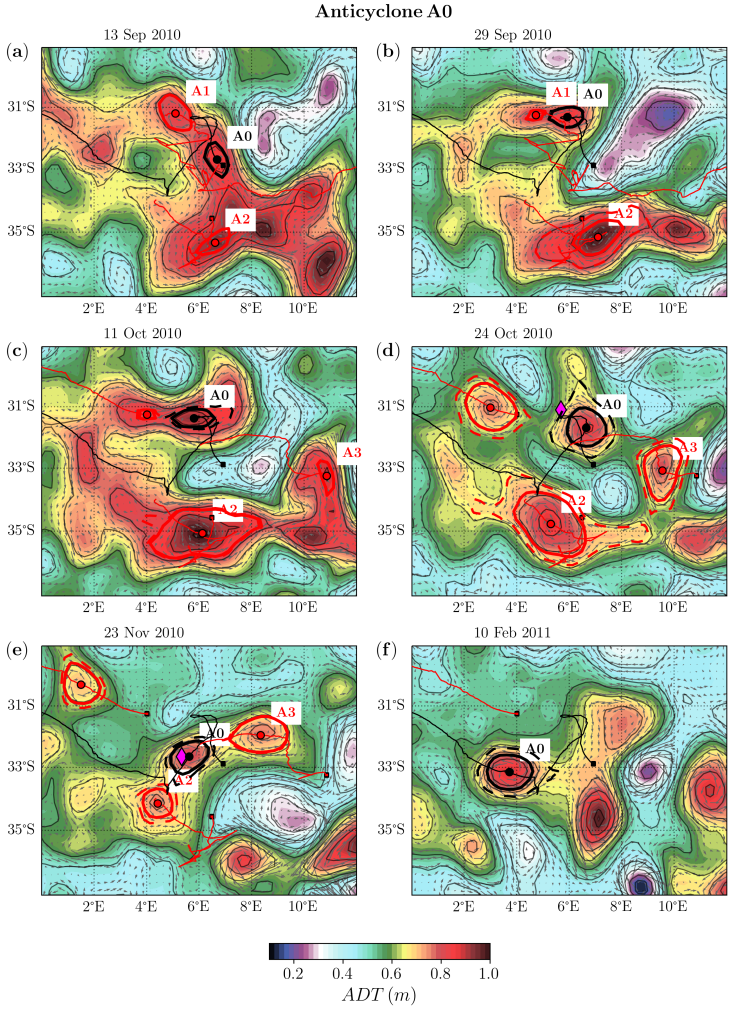

Figure 10. Snapshots along the temporal evolution of anticyclone A0 (panels **a**–**f**) propagating westward in the Southern Ocean. The background colors correspond to the ADT (m) fields while the gray arrows correspond to surface geostrophic velocities. The characteristic and outer contours as detected by TOEddies are shown in the black solid and dashed lines. The Argo floats trapped in the eddies are shown with the magenta diamond points.

Figure 12e presents the temporal evolution of the temperature anomaly of the eddy A0 from Argo floats trapped within its core from 24 October 2010 to 08 June 2013. Only profiles situated within the outermost radius of the eddy from its center were selected (Figure 9a). The integration of Argo vertical profiles with the eddy detection based on satellite altimetry suggests that A0 is not undergoing dissipation. Instead, the data suggest that the eddy is experiencing a progressive deepening of its vertical structure and a clear separation from the ocean surface. Dynamical topography results from the vertical integration of the thermohaline properties of the water column. A reduction in eddy intensity may be linked to alterations in the thermohaline properties of the upper water column through eddy cooling, as observed by Arhan et al. [58], or eddy subsidence at depth (as in this case). The latter case was initially documented for another Agulhas Ring in [5,40], showing that the eddy subducted to become an intensified subsurface eddy. Therefore, when the eddy signal disappears from altimetry maps, it is possible that it has not simply dissipated. Instead, it may indicate that the eddy has penetrated more deeply and become disconnected from the surface.

Meanwhile, the cyclone C0 was initially identified by TOEddies on 24 June 2011, off the western coast of Australia (112.9°E, 27.57°S), and was subsequently tracked as it propagated southwestward into the Indian Ocean for a period exceeding four years. The reconstruction of the TOEddies network also revealed multiple instances of merging and splitting along this cyclonic eddy trajectory. A few months after its formation, on 25 February 2012, a merging event (Figure 11b) was detected with a short-lived cyclone (less than a month). On 9 January 2013 (Figure 11d), C0 merged with another cyclonic eddy that originated from the western border of Australia and propagated westward. By 14 June 2014, C0 had already drifted 2226 km, while being sampled by 22 different Argo floats, providing 138 vertical profiles at varying radial distances from the center of the eddy (magenta dots in Figure 9b). On 7 February 2016, the eddy reached 61.28°E, 37.58°S and merged with another cyclone, which continued its westward propagation till 26 February 2018, reaching 33.82°E, 33.93°S.

To facilitate comparison between datasets, we located cyclone C0 in the META3.2, TIAN, and GOMEAD atlases. The META3.2 dataset identified three separate cyclones (instead of one) that appear to be following a similar westward trajectory, as illustrated in Figure 9j. The second cyclone in the META3.2 dataset was identified just a few days after the last detection of the first cyclone in the same dataset. The TOEddies identified this interaction as a merging of two cyclones. Similarly, cyclone C0 in the TIAN dataset was identified as two distinct cyclonic eddies with no prior connection between them. The TIAN atlas was unable to link the two trajectories due to a significant variation in eddy size during the period in question (25 August 2012). Furthermore, the eddy velocity was found to be slightly lower (0.12 m/s) in intensity compared to that of TOEddies. GOMEAD also classified these cyclones as two distinct eddies, though with shorter trajectories.

Figure 12b,d,f provides an illustration of the value of integrating satellite altimetry data with the eddy subsurface properties derived from the extensive Argo vertical profiles. This approach offers a more comprehensive understanding of the dynamics and evolution of eddies. The figure illustrates the presence of a pronounced inverted temperature anomaly signal in the upper layers for C0. Furthermore, the analyzed data indicate that the core of A0 is situated between 200 and 1000 m, exhibiting consistent and markedly distinct properties that are largely independent of seasonal variations in the mixing layer. The presented evidence suggests that these eddies are subsurface-intensified. These findings are consistent with those of previous studies that employed the TOEddies atlas to examine a range of Atlantic eddies [5,7,40]. These examples demonstrate the necessity of this integrated approach to fully grasp the complex vertical and horizontal structure of mesoscale eddies, particularly when considering their role in large-scale oceanic exchanges. Future work will aim to explore these vertical structures in more detail, including their interactions with subsurface topography, to gain a deeper understanding of their dynamical behavior throughout their life cycle.

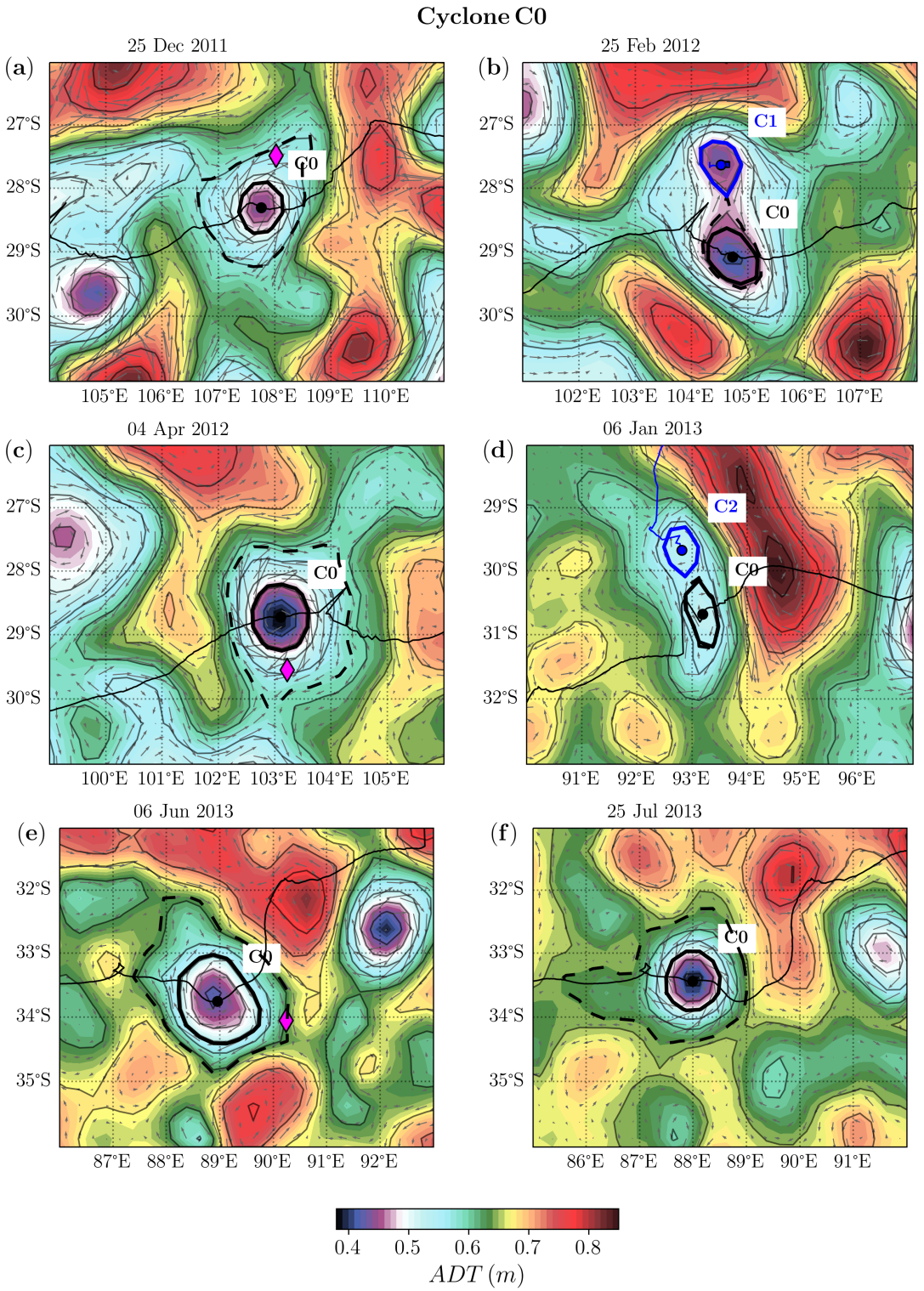

Figure 11. Snapshots along the temporal evolution of cyclone C0 (panels **a**–**f**) propagating westward in the Indian Ocean. The background colors correspond to the ADT (m) fields while the gray arrows correspond to surface geostrophic velocities. The characteristic and outer contours as detected by TOEddies are shown in the black solid and dashed lines. The Argo floats trapped in the eddies are shown with magenta diamond points.

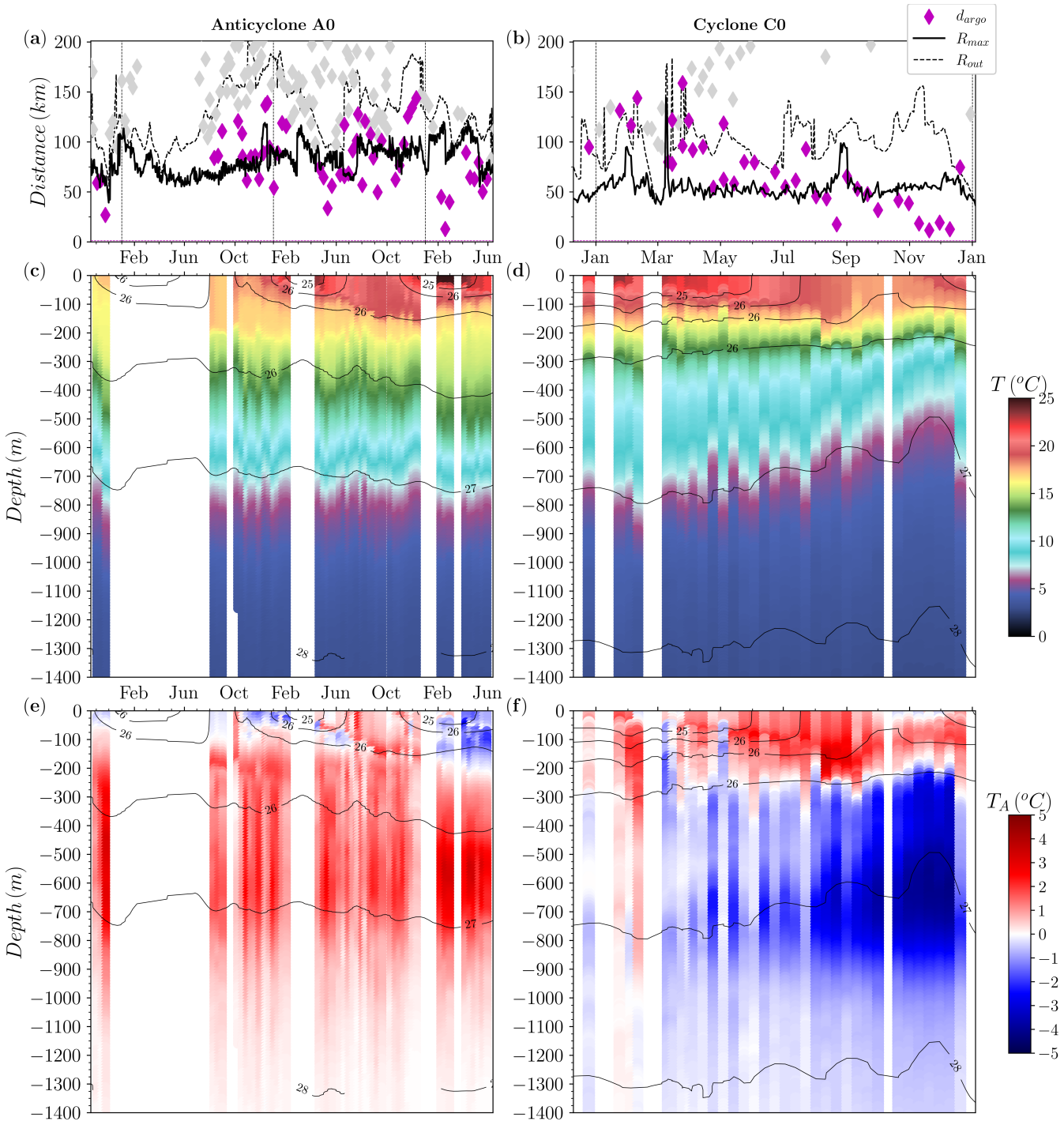

Figure 12. Temporal evolution of anticyclone A0 and cyclone C0 vertical structures as obtained by Argo floats trapped inside the eddy core ($d_{ARGO} \leq Rmax$) (shown as magenta points in panels (**a**,**b**). Vertical profiles of temperature T (°C) and temperature anomalies T_A (°C) are shown in panels (**c**,**e**) for anticyclone A0, and in panels (**d**,**f**) for cyclone C0.

4. Conclusions

In this study, we introduced a new global atlas [37] of mesoscale eddies, built using an advanced version of the TOEddies algorithm. TOEddies distinguishes itself from other global eddy atlases by operating directly on absolute dynamic topography (ADT) fields without spatial filtering, detecting eddy networks that reflect complex merging and splitting behaviors, and incorporating in situ Argo float measurements for a more

comprehensive view of the eddy structure and subsurface characteristics. By comparing TOEddies with other leading global datasets [4,34,38,39], we highlight the strengths and limitations of different detection methodologies and illustrate how TOEddies enables a deeper understanding of mesoscale ocean dynamics.

Across all datasets, our analysis confirms several well-documented mesoscale eddy behaviors. Over 80% of eddies display westward propagation, driven by the beta effect, while their trajectories reveal a distinct northward deflection of anticyclonic eddies and a southward deflection of cyclonic eddies, consistent with prior studies [10,55,56,59]. Despite these consistencies, the specific characteristics of eddies—such as count, size, and intensity—vary among datasets, as each utilizes unique detection and tracking criteria. For instance, analyses reveal that employing unfiltered ADT rather than SLA or filtered ADT fields consistently provides more robust estimates of eddy intensities. While these methods tend to underestimate these values, the TOEddies algorithm produces an eddy radius that better matches the expected natural spatial variability (a metric of which is provided by the first internal baroclinic Rossby radius).

Notably, TOEddies uniquely captures complex eddy interactions, constructing eddy trajectories as interconnected networks rather than isolated paths. These interactions redefine traditional perspectives of eddy life cycles, showing that eddies frequently merge, split, and interact dynamically with neighboring structures. Furthermore, this atlas allows us to capture longer-lived eddies with lifetimes exceeding 1.5 years, particularly in anticyclonic structures. Our analysis underscores that anticyclones generally maintain more stable, coherent structures compared to cyclones, aligning with earlier observations of global asymmetry [60–62]. This longevity may reflect the visibility of anticyclonic eddies in satellite altimetry, even as they subduct into the subsurface, a phenomenon frequently documented in regions like the Agulhas Current System [4,5,7,40].

By integrating TOEddies with Argo float profiles, we highlight critical discrepancies between surface and subsurface eddy dynamics. Instances of attenuation in surface anomalies with persistence in deeper layers reveal limitations in inferring eddy evolution solely from surface altimetry. These results emphasize the importance of combining satellite data with in situ observations for a more complete understanding of eddy dynamics. In particular, subsurface processes like subduction may introduce observational biases, leading to an under-representation of cyclonic eddies in satellite-derived datasets.

TOEddies provides a unique resource that enhances our ability to characterize eddies not only as isolated structures but as interconnected, dynamic entities within turbulent ocean fields. Its detailed accounting of eddy merging and splitting events challenges the conventional one-eddy, one-trajectory model, showing instead that mesoscale eddies interact dynamically with their surroundings. These interactions have implications for the pathways and lifetimes of eddy networks and for the understanding of eddy-driven water mass transport. This new atlas thus stands as a valuable tool for the oceanographic community, providing an accessible, rich dataset for studies on ocean dynamics, climate variability, and marine ecosystem processes.

Supplementary Materials: The following supporting information can be downloaded at: https://www.mdpi.com/article/10.3390/rs16224336/s1.

Author Contributions: A.I. and S.S. designed the study and contributed to the writing. A.I. performed the data analysis while R.L. and L.G. created and provided the TOEddies dataset and automatic eddy detection for the study area. All authors have read and agreed to the published version of the manuscript.

Funding: This paper was supported by the TRIATLAS project, which has received funding from the European Union's Horizon 2020 research and innovation program under grant agreement No 817578 with additional support from CNES (the French National Center for Space Studies) through the TOEddies, and EUREC4A-OA proposals.

Data Availability Statement: The Ssalto/Duacs altimeter products were produced and distributed by the Copernicus Marine and Environment Monitoring Service (CMEMS) (https://marine.copernicus.

eu/, accessed on 5 November 2024). The Argo data were collected and made freely available by the International Argo Program and the national programs that contribute to it (https://coriolis.eu.org, accessed on 5 November 2024). The TOEddies global atlas data used for this paper are publicly available at SEANOE, TOEddies Global Mesoscale Eddy Atlas Colocated with Argo Float Profiles, at https://doi.org/10.17882/102877, accessed on 5 November 2024. Data from other atlases were obtained by accessing the corresponding publication links, as provided by the respective papers.

Acknowledgments: This work was supported by the European Union's Horizon 2020 research and innovation program under grant agreements no. 817578 (TRIATLAS), the TOEddies and BIOSWOT CApeCauldron CNES-TOSCA and the ENS Chaire Chanel research grants. We also acknowledge the mesoscale calculation server CICLAD (http://ciclad-web.ipsl.jussieu.fr, accessed on 5 November 2024) dedicated to Institut Pierre Simon Laplace modeling effort for technical and computational support.

Conflicts of Interest: The authors declare that the research was conducted in the absence of any commercial or financial relationships that could be construed as potential conflicts of interest.

Appendix A.

Appendix A.1. TOEddies Eddy Detection

To identify and characterize the outermost contours of absolute dynamic topography (ADT) around local extrema, TOEddies approximates contours as polygons, with vertices aligned with the grid lines of the ADT field. Given an extremum E, an outermost contour C surrounding E is defined by the following criteria:

- C is a closed isoline of ADT;
- C contains extremum E;
- C does not contain any extremum of opposite sign;
- C has a minimum area of $\pi(25\,\mathrm{km})^2$;
- The absolute value of the difference between the ADT level of C and the ADT of E is greater than 1 mm; this threshold difference is called the persistence parameter;
- C does not contain any extremum other than E with the same sign as E and with an associated outermost contour;
- No isoline exterior to C has the above properties.

This definition is recursive in its sixth point so it is not complete. We complete the definition by adding that the minima of ADT are examined in descending order of ADT and the maxima in ascending order. After identifying the outermost contour C around an extremum E, TOEddies also detects the "maximum-speed contour", a closed ADT isoline containing E and situated within C that maximizes the mean azimuthal speed. This speed at each point on the contour is computed as

$$V_\theta = \frac{xv - yu}{\sqrt{x^2 + y^2}}$$

where

$$x = \cos\phi_E \, (\lambda - \lambda_E)$$
$$y = \phi - \phi_E$$

(u, v) is the geostrophic speed at the point (λ, ϕ) on the contour, and (λ_E, ϕ_E) is the position of the extremum. This process results in two distinct contours for each extremum, the outermost contour, delineating the eddy's boundary, and the maximum-speed contour, which encloses the eddy's dynamical core. The eddy's size is then determined by calculating the radius of a circle covering the area bounded by these contours, yielding two distinct average radii: $\langle R_{max} \rangle$ for the maximum radius and $\langle R_{out} \rangle$ for the outer characteristic eddy radius.

Appendix A.2. TOEddies Eddy Tracking

In TOEddies, the overlapping criterion is applied firstly to the maximum-speed contours and then to the outermost contours. Two instantaneous eddies overlap if they are between 1 and 5 days apart and if the area of the intersection of their maximum-speed or outermost contours is greater than 50% of the minimum of the areas of the contours. An eddy can overlap with more than one other eddy.

A given eddy can even have several successors (overlapping eddies at subsequent dates) at different dates or several predecessors (overlapping eddies at previous dates) at different dates. However, if an eddy has a successor at time distance δ, then we restrict the search for successors at time distances greater than δ: an eddy at distance $\delta' > \delta$ can only be a successor if it has no predecessor at distance $< \delta'$.

Thus, TOEddies creates, for each polarity (anticyclones and cyclones) an abstract graph in which each node is an instantaneous eddy and there is an edge between two nodes if the instantaneous eddies overlap. The edges have the time direction so the graph is directed acyclic. Splitting of eddies appears in the graph as nodes with an out-degree ≥ 2 and merging of eddies appears as nodes with an in-degree ≥ 2. For each polarity, the graph has about 3×10^7 nodes and 3×10^7 edges.

TOEddies proceeds by collapsing the graph of instantaneous eddies into a "graph of segments". A segment is a sequence of nodes in the graph of instantaneous eddies without splitting, except maybe at the last node of the segment, and without merging, except maybe at the first node of the segment. In the graph of segments, each node is a segment and edges correspond to splitting or merging events.

For each edge in the graph of segments, TOEddies computes a cost:

$$C = \sqrt{\left(\frac{d - \bar{d}}{\sigma_d}\right)^2 + \left(\frac{\Delta N - \overline{\Delta N}}{\sigma_{\Delta N}}\right)^2 + \left(\frac{\Delta r - \overline{\Delta r}}{\sigma_{\Delta r}}\right)^2}$$

where d is the distance between the extremum of the last eddy in the head segment of the edge and the extremum of the first eddy in the tail segment of the edge,

$$\Delta N = N_{\text{Ro,first}}(\text{tail segment}) - N_{\text{Ro,last}}(\text{head segment})$$

$$\Delta r = r_{\text{first}}(\text{tail segment}) - r_{\text{last}}(\text{head segment})$$

$N_{\text{Ro,first}}(\text{segment})$ is the mean on the first seven days of the segment of the Rossby number associated to the maximum-speed contour. $r_{\text{first}}(\text{segment})$ is the mean on the first seven days of the segment of the radius of the maximum-speed contour (that is, the radius of the equal-area disk). Similarly, $N_{\text{Ro,last}}(\text{segment})$ and $r_{\text{last}}(\text{segment})$ are mean values on the last seven days of the segment.

From the graph of segments weighted by cost values, TOEddies computes eddy trajectories. A trajectory is a path in the graph of segments. Each non-root node in the graph has a closest predecessor: the head of the in-edge with the lowest cost. Each non-leaf mode in the graph has a closest successor: the tail of the out-edge with the lowest cost. In order to construct trajectories, TOEddies processes the nodes in topological order. For each node, TOEddies looks whether the node is the closest successor of its closest predecessor. If so, then this node is placed in the same trajectory as its closest predecessor; else this node begins a new trajectory. Because of "phantom instantaneous eddies", detected from the Aviso dataset, but not real, there are patterns in the graph of segments where a splitting is immediately followed by a merging. We do not want to let those phantom patterns interrupt trajectories so we detect those patterns in the graph: if the merging is 6 days or less after the splitting, then the trajectory continues through the pattern, going through the shortest (that is, with the smallest cost) branch of the splitting–merging.

References

1. Schütte, F.; Brandt, P.; Karstensen, J. Occurrence and characteristics of mesoscale eddies in the tropical northeastern Atlantic Ocean. *Ocean. Sci.* **2016**, *12*, 663–685. [CrossRef]
2. Schütte, F.; Karstensen, J.; Krahmann, G.; Hauss, H.; Fiedler, B.; Brandt, P.; Visbeck, M.; Körtzinger, A. Characterization of 'dead-zone' eddies in the eastern tropical North Atlantic. *Biogeosciences* **2016**, *13*, 5865–5881. [CrossRef]
3. Karstensen, J.; Schütte, F.; Pietri, A.; Krahmann, G.; Fiedler, B.; Grundle, D.; Hauss, H.; Körtzinger, A.; Lüscher, C.R.; Testor, P.; et al. Upwelling and isolation in oxygen-depleted anticyclonic modewater eddies and implications for nitrate cycling. *Biogeosciences* **2017**, *14*, 2167–2181. [CrossRef]
4. Laxenaire, R.; Speich, S.; Blanke, B.; Chaigneau, A.; Pegliasco, C.; Stegner, A. Anticyclonic Eddies Connecting the Western Boundaries of Indian and Atlantic Oceans. *J. Geophys. Res. Ocean.* **2018**, *123*, 7651–7677. [CrossRef]
5. Laxenaire, R.; Speich, S.; Stegner, A. Evolution of the Thermohaline Structure of One Agulhas Ring Reconstructed from Satellite Altimetry and Argo Floats. *J. Geophys. Res.* **2019**, *124*, 8969–9003. [CrossRef]
6. Ioannou, A.; Stegner, A.; Le Vu, B.; Taupier-Letage, I.; Speich, S. Dynamical Evolution of Intense Ierapetra Eddies on a 22 Year Long Period. *J. Geophys. Res. Ocean.* **2017**, *122*, 9276–9298. [CrossRef]
7. Ioannou, A.; Speich, S.; Laxenaire, R. Characterizing Mesoscale Eddies of Eastern Upwelling Origins in the Atlantic Ocean and Their Role in Offshore Transport. *Front. Mar. Sci.* **2022**, *9*, 835260. [CrossRef]
8. Nencioli, F.; Olmo, G.D.; Quartly, G.D. Agulhas Ring Transport Efficiency from Combined Satellite Altimetry and Argo Profiles. *J. Geophys. Res. Ocean.* **2018**, *123*, 5874–5888. [CrossRef]
9. Flierl, G.R. Particle motions in large-amplitude wave fields. *Geophys. Astrophys. Fluid Dyn.* **1981**, *18*, 39–74. [CrossRef]
10. Chelton, D.B.; Schlax, M.G.; Samelson, R.M. Global observations of nonlinear mesoscale eddies. *Prog. Oceanogr.* **2011**, *91*, 167–216. [CrossRef]
11. Sato, O.T.; Polito, P.S. Observation of South Atlantic subtropical mode waters with Argo profiling float data. *J. Geophys. Res. Ocean.* **2014**, *119*, 2860–2881. [CrossRef]
12. McGillicuddy, D.J.; Anderson, L.A.; Bates, N.R.; Bibby, T.; Buesseler, K.O.; Carlson, C.A.; Davis, C.S.; Ewart, C.; Falkowski, P.G.; Goldthwait, S.A.; et al. Eddy/Wind Interactions Stimulate Extraordinary Mid-Ocean Plankton Blooms. *Science* **2007**, *316*, 1021–1026. [CrossRef] [PubMed]
13. Villar, E.; Farrant, G.K.; Follows, M.; Garczarek, L.; Speich, S.; Audic, S.; Bittner, L.; Blanke, B.; Brum, J.R.; Brunet, C.; et al. Ocean plankton. Environmental characteristics of Agulhas rings affect interocean plankton transport. *Science* **2015**, *348*, 1261447–1261447. [CrossRef] [PubMed]
14. Dufois, F.; Hardman-Mountford, N.J.; Greenwood, J.; Richardson, A.J.; Feng, M.; Matear, R.J. Anticyclonic eddies are more productive than cyclonic eddies in subtropical gyres because of winter mixing. *Sci. Adv.* **2016**, *2*, e1600282. [CrossRef]
15. Cornec, M.; Laxenaire, R.; Speich, S.; Claustre, H. Impact of Mesoscale Eddies on Deep Chlorophyll Maxima. *Geophys. Res. Lett.* **2021**, *48*, e2021GL093470. [CrossRef]
16. Cornec, M.; Claustre, H.; Mignot, A.; Guidi, L.; Lacour, L.; Poteau, A.; D'Ortenzio, F.; Gentili, B.; Schmechtig, C. Deep Chlorophyll Maxima in the Global Ocean: Occurrences, Drivers and Characteristics. *Glob. Biogeochem. Cycles* **2021**, *35*, e2020GB006759. [CrossRef]
17. LeTraon, P.Y.; Nadal, F.; Ducet, N. An Improved Mapping Method of Multisatellite Altimeter Data. *J. Atmos. Ocean. Technol.* **1998**, *15*, 522–533. [CrossRef]
18. Amores, A.; Jordà, G.; Arsouze, T.; Le Sommer, J. Up to What Extent Can We Characterize Ocean Eddies Using Present-Day Gridded Altimetric Products? *J. Geophys. Res. Ocean.* **2018**, *123*, 7220–7236. [CrossRef]
19. Khachatrian, E.; Sandalyuk, N.; Lozou, P. Eddy Detection in the Marginal Ice Zone with Sentinel-1 Data Using YOLOv5. *Remote. Sens.* **2023**, *15*, 2244. [CrossRef]
20. Kozlov, I.E.; Atadzhanova, O.A. Eddies in the Marginal Ice Zone of Fram Strait and Svalbard from Spaceborne SAR Observations in Winter. *Remote Sens.* **2022**, *14*, 134. [CrossRef]
21. Xia, L.; Chen, G.; Chen, X.; Ge, L.; Huang, B. Submesoscale oceanic eddy detection in SAR images using context and edge association network. *Front. Mar. Sci.* **2019**, *9*, 1023624. [CrossRef]
22. Manta, G.; Speich, S.; Karstensen, J.; Hummels, R.; Kersalé, M.; Laxenaire, R.; Piola, A.; Chidichimo, M.P.; Sato, O.T.; da Cunha, L.C.; et al. The South Atlantic Meridional Overturning Circulation and Mesoscale Eddies in the First GO-SHIP Section at 34.5°S. *J. Geophys. Res. Ocean.* **2021**, *126*, e2020JC016962. [CrossRef]
23. Stevens, B.; Bony, S.; Farrell, D.; Ament, F.; Blyth, A.; Fairall, C.; Karstensen, J.; Quinn, P.K.; Speich, S.; Acquistapace, C.; et al. EUREC^{4}A. *Earth Syst. Sci. Data* **2021**, *13*, 4067–4119. [CrossRef]
24. Subirade, C.; L'Hégaret, P.; Speich, S.; Laxenaire, R.; Karstensen, J.; Carton, X. Combining an Eddy Detection Algorithm with In-Situ Measurements to Study North Brazil Current Rings. *Remote Sens.* **2023**, *15*, 1897. [CrossRef]
25. Chelton, D.B.; Schlax, M.G.; Samelson, R.M.; de Szoeke, R.A. Global observations of large oceanic eddies. *Geophys. Res. Lett.* **2007**, *34*, L15606. [CrossRef]
26. Schlax, M.G.; Chelton, D.B. The "Growing Method" of Eddy Identification and Tracking in Two and Three Dimensions. 2016. Available online: https://api.semanticscholar.org/CorpusID:53683135 (accessed on 1 March 2022).
27. Faghmous, J.H.; Frenger, I.; Yao, Y.; Warmka, R.; Lindell, A.; Kumar, V. A daily global mesoscale ocean eddy dataset from satellite altimetry. *Sci. Data* **2015**, *2*, 150028. [CrossRef]

28. Mkhinini, N.; Coimbra, A.L.S.; Stegner, A.; Arsouze, T.; Taupier-Letage, I.; Béranger, K. Long-lived mesoscale eddies in the eastern Mediterranean Sea: Analysis of 20 years of AVISO geostrophic velocities. *J. Geophys. Res. Ocean.* **2014**, *119*, 8603–8626. [CrossRef]
29. Halo, I.; Backeberg, B.; Penven, P.; Ansorge, I.; Reason, C.; Ullgren, J. Eddy properties in the Mozambique Channel: A comparison between observations and two numerical ocean circulation models. *Deep-Sea Res. II* **2014**, *100*, 38–53. [CrossRef]
30. Le Vu, B.; Stegner, A.; Arsouze, T. Angular Momentum Eddy Detection and Tracking Algorithm (AMEDA) and Its Application to Coastal Eddy Formation. *J. Atmos. Ocean. Technol.* **2018**, *35*, 739–762. [CrossRef]
31. Doglioli, A.; Blanke, B.; Speich, S.; Lapeyre, G. Tracking coherent structures in a regional ocean model with wavelet analysis: Application to Cape Basin Eddies. *J. Geophys. Res.* **2007**, *112*, C05043. [CrossRef]
32. Mason, E.; Pascual, A.; McWilliams, J.C. A New Sea Surface Height Based Code for Oceanic Mesoscale Eddy Tracking. *J. Atmos. Ocean. Technol.* **2014**, *31*, 1181–1188. [CrossRef]
33. Nencioli, F.; Dong, C.; Dickey, T.; Washburn, L.; McWilliams, J. A vector geometry-based eddy detection algorithm and its application to a high-resolution numerical model product and high-frequency radar surface velocities in the Southern California Bight. *J. Atmos. Ocean. Technol.* **2010**, *27*, 564–579. [CrossRef]
34. Pegliasco, C.; Delepoulle, A.; Mason, E.; Morrow, R.; Faugère, Y.; Dibarboure, G. META3.1exp: A new global mesoscale eddy trajectory atlas derived from altimetry. *Earth Syst. Sci. Data* **2022**, *14*, 1087–1107. [CrossRef]
35. Du, Y.; Yi, J.; Wu, D.; He, Z.; Wang, D.; Fuyuan, L. Mesoscale oceanic eddies in the South China Sea from 1992 to 2012: Evolution processes and statistical analysis. *Acta Oceanol. Sin.* **2014**, *33*, 36–47. [CrossRef]
36. Cui, W.; Wang, W.; Zhang, J.; Yang, J. Multicore structures and the splitting and merging of eddies in global oceans from satellite altimeter data. *Ocean Sci.* **2019**, *15*, 413–430. [CrossRef]
37. Laxenaire, R.; Guez, L.; Chaigneau, A.; Isic, M.; Ioannou, A.; Speich, S. *TOEddies Global Mesoscale Eddy Atlas Colocated with Argo Float Profiles*; SEANOE: Brest, France, 2024. [CrossRef]
38. Tian, F.; Wu, D.; Yuan, L.; Chen, G. Impacts of the efficiencies of identification and tracking algorithms on the statistical properties of global mesoscale eddies using merged altimeter data. *Int. J. Remote. Sens.* **2019**, *41*, 2835–2860. [CrossRef]
39. Dong, C.; Liu, L.; Nencioli, F.; Bethel, B.J.; Liu, Y.; Xu, G.; Ma, J.; Ji, J.; Sun, W.; Shan, H.; et al. The near-global ocean mesoscale eddy atmospheric-oceanic-biological interaction observational dataset. *Sci. Data* **2022**, *9*, 436. [CrossRef]
40. Laxenaire, R.; Speich, S.; Stegner, A. Agulhas Ring Heat Content and Transport in the South Atlantic Estimated by Combining Satellite Altimetry and Argo Profiling Floats Data. *J. Geophys. Res. Ocean.* **2020**, *125*, e2019JC015511. [CrossRef]
41. Kersalé, M.; Lamont, T.; Speich, S.; Terre, T.; Laxenaire, R.; Roberts, M.J.; van den Berg, M.A.; Ansorge, I.J. Moored observations of mesoscale features in the Cape Basin: characteristics and local impacts on water mass distributions. *Ocean Sci.* **2018**, *14*, 923–945. [CrossRef]
42. Capuano, T.A.; Speich, S.; Carton, X.; Laxenaire, R. Indo-Atlantic Exchange, Mesoscale Dynamics, and Antarctic Intermediate Water. *J. Geophys. Res. Ocean.* **2018**, *123*, 1–22. [CrossRef]
43. Foltz, G.R.; Brandt, P.; Richter, I.; Rodríguez-Fonseca, B.; Hernandez, F.; Dengler, M.; Rodrigues, R.R.; Schmidt, J.O.; Yu, L.; Lefevre, N.; et al. The Tropical Atlantic Observing System. *Front. Mar. Sci.* **2019**, *6*, 206. [CrossRef]
44. Shropshire, T.A.; Morey, S.L.; Chassignet, E.P.; Bozec, A.; Coles, V.J.; Landry, M.R.; Swalethorp, R.; Zapfe, G.; Stukel, M.R. Quantifying spatiotemporal variability in zooplankton dynamics in the Gulf of Mexico with a physical–biogeochemical model. *Biogeosciences* **2020**, *17*, 3385–3407. [CrossRef]
45. Stephan, C.C.; Schnitt, S.; Schulz, H.; Bellenger, H.; de Szoeke, S.P.; Acquistapace, C.; Baier, K.; Dauhut, T.; Laxenaire, R.; Morfa-Avalos, Y.; et al. Ship- and island-based atmospheric soundings from the 2020 EUREC4A field campaign. *Earth Syst. Sci. Data* **2021**, *13*, 491–514. [CrossRef]
46. Chen, Y.; Speich, S.; Laxenaire, R. Formation and Transport of the South Atlantic Subtropical Mode Water in Eddy-Permitting Observations. *J. Geophys. Res. Ocean.* **2021**, *127*, 2169–9275. [CrossRef]
47. Manta, G.; Speich, S.; Barreiro, M.; Trinchin, R.; de Mello, C.; Laxenaire, R.; Piola, A.R. Shelf Water Export at the Brazil-Malvinas Confluence Evidenced from Combined in situ and Satellite Observations. *Front. Mar. Sci.* **2022**, *9*, 857594. [CrossRef]
48. Olivier, L.; Boutin, J.; Reverdin, G.; Lefèvre, N.; Landschützer, P.; Speich, S.; Karstensen, J.; Labaste, M.; Noisel, C.; Ritschel, M.; et al. Wintertime process study of the North Brazil Current rings reveals the region as a larger sink for CO_2 than expected. *Biogeosciences* **2022**, *19*, 2969–2988. [CrossRef]
49. Baudena, A.; Laxenaire, R.; Catalano, C.; Claustre, H.; Ioannou, A.; Leymarie, E.; Picheral, M.; Poteau, A.; Speich, S.; Stemmann, L.; et al. A Lagrangian perspective on the carbon and oxygen budget of an oceanic eddy. *Res. Sq.* 2023, *preprint*. [CrossRef]
50. Speich, S. The Embarked Science Team. EUREC4A-OA. Cruise Report. 19 January—19 February 2020. Vessel: L'ATALANTE. Mission Report, 2021. [CrossRef]
51. Olivier, L.; Reverdin, G.; Boutin, J.; Laxenaire, R.; Iudicone, D.; Pesant, S.; Calil, P.H.; Horstmann, J.; Couet, D.; Erta, J.; et al. Late summer northwestward Amazon plume pathway under the action of the North Brazil Current rings. *Remote. Sens. Environ.* **2024**, *307*, 114165. [CrossRef]
52. Lumpkin, R. Global characteristics of coherent vortices from surface drifter trajectories. *J. Geophys. Res. Ocean.* **2016**, *121*, 1306–1321. [CrossRef]
53. Pegliasco, C.; Chaigneau, A.; Morrow, R. Main eddy vertical structures observed in the four major Eastern Boundary Upwelling Systems. *J. Geophys. Res. Ocean.* **2015**, *120*, 6008–6033. [CrossRef]

54. Chelton, D.B.; deSzoeke, R.A.; Schlax, M.G.; Naggar, K.E.; Siwertz, N. Geographical Variability of the First Baroclinic Rossby Radius of Deformation. *J. Phys. Oceanogr.* **1998**, *28*, 433–460. [CrossRef]
55. Cushman-Roisin, B.; Tang, B.; Chassignet, E.P. Westward Motion of Mesoscale Eddies. *J. Phys. Oceanogr.* **1990**, *20*, 758–768. [CrossRef]
56. Morrow, R. Divergent pathways of cyclonic and anti-cyclonic ocean eddies. *Geophys. Res. Lett.* **2004**, *31*, L24311. [CrossRef]
57. Lehahn, Y.; d'Ovidio, F.; Lévy, M.; Amitai, Y.; Heifetz, E. Long range transport of a quasi isolated chlorophyll patch by an Agulhas ring. *Geophys. Res. Lett.* **2011**, *38*, L16610. [CrossRef]
58. Arhan, M.; Speich, S.; Messager, C.; Dencausse, G.; Fine, R.; Boye, M. Anticyclonic and cyclonic eddies of subtropical origin in the subantarctic zone south of Africa. *J. Geophys. Res. Ocean.* **2011**, *116*, C11004. [CrossRef]
59. Chaigneau, A.; Gizolme, A.; Grados, C. Mesoscale eddies off Peru in altimeter records: Identification algorithms and eddy spatio-temporal patterns. *Prog. Oceanogr.* **2008**, *79*, 106–119. [CrossRef]
60. Poulin, F.; Flierl, G. The Nonlinear Evolution of Barotropically Unstable Jets. *J. Phys. Oceanogr.* **2003**, *33*, 2173–2192. [CrossRef]
61. Perret, G.; Dubos, T.; Stegner, A. How Large-Scale and Cyclogeostrophic Barotropic Instabilities Favor the Formation of Anticyclonic Vortices in the Ocean. *J. Phys. Oceanogr.* **2011**, *41*, 303–328. [CrossRef]
62. Ioannou, A.; Stegner, A.; Dubos, T.; Le Vu, B.; Speich, S. Generation and Intensification of Mesoscale Anticyclones by Orographic Wind Jets: The Case of Ierapetra Eddies Forced by the Etesians. *J. Geophys. Res. Ocean.* **2020**, *125*, e2019JC015810. [CrossRef]